MNRAS **000**, 1–15 (2016) Preprint 20 December 2016 Compiled using MNRAS LATEX style file v3.0

Rise and fall of the dust shell of the classical nova V339 Delphini

A. Evans[1⋆], D. P. K. Banerjee[2], R. D. Gehrz[3], V. Joshi[2], N. M. Ashok[2], V. A. R. M. Ribeiro[4], M. J. Darnley[5], C. E. Woodward[3], D. Sand[6], G. H. Marion[7], T. R. Diamond[8], S. P. S. Eyres[9], R. M. Wagner[10], L. A. Helton[11], S. Starrfield[12], D. P. Shenoy[3], J. Krautter[13], W. D. Vacca[11], M. T. Rushton[14]

[1]*Astrophysics Group, Keele University, Keele, Staffordshire, ST5 5BG, UK*
[2]*Physical Research Laboratory, Ahmedabad 380009, India*
[3]*Minnesota Institute for Astrophysics, School of Physics & Astronomy 116 Church Street SE, University of Minnesota, Minneapolis, MN 55455, USA*
[4]*Department of Astrophysics/IMAPP, Radboud University, P.O. Box 9010, 6500 GL Nijmegen, The Netherlands and Department of Physics and Astronomy, Botswana International University of Science and Technology, Private Bag 16, Palapye, Botswana*
[5]*Astrophysics Research Institute, Liverpool John Moores University, IC2 Liverpool Science Park, Liverpool, L3 5RF, UK*
[6]*Department of Physics, Texas Tech University, Lubbock, TX 79409, USA*
[7]*University of Texas at Austin, 1 University Station C1400, Austin, TX 78712-0259, USA*
[8]*NASA Goddard Space Flight Center, Greenbelt, MD 20771, USA*
[9]*Jeremiah Horrocks Institute, University of Central Lancashire, Preston PR1 2HE, UK*
[10]*Department of Astronomy, The Ohio State University, 140 West 18th Avenue, Columbus, OH 43210, USA and LBT Observatory, University of Arizona, Tucson, AZ 85721-0065, USA*
[11]*USRA-SOFIA Science Center, NASA Ames Research Center, Moffett Field, CA 94035, USA*
[12]*School of Earth and Space Exploration, Arizona State University, Box 871404, Tempe, AZ 85287-1404, USA*
[13]*Landessternwarte-Zentrum für Astronomie der Universität, Königstuhl, D-69117 Heidelberg, Germany*
[14]*Astronomical Institute of the Romanian Academy, Str. Cutitul de Argint 5, Bucharest, 040557, Romania*

Version SUB (20 December 2016)

ABSTRACT

We present infrared spectroscopy of the classical nova V339 Del, obtained over a $\sim$ 2 year period. The infrared emission lines were initially symmetrical, with HWHM velocities of 525 km s^{-1}. In later ($t \gtrsim 77$days, where t is the time from outburst) spectra however, the lines displayed a distinct asymmetry, with a much stronger blue wing, possibly due to obscuration of the receding component by dust. Dust formation commenced at $\sim$ day 34.75 at a condensation temperature of 1480 ± 20 K, consistent with graphitic carbon. Thereafter the dust temperature declined with time as $T_{\rm d} \propto t^{-0.346}$, also consistent with graphitic carbon. The mass of dust initally rose, as a result of an increase in grain size and/or number, peaked at $\sim$ day 100, and then declined precipitously. This decline was most likely caused by grain shattering due to electrostatic stress after the dust was exposed to X-radiation. An Appendix summarises Planck Means for carbon, and the determination of grain mass and radius for a carbon dust shell.

Key words: line: profiles – infrared: stars – novae, cataclysmic variables – circumstellar matter – stars: individual: V339 Del

1 INTRODUCTION

Classical nova (CN) eruptions are produced by a thermonuclear runaway (TNR) on the surface of a white dwarf (WD) that has been accreting material from a companion star in a semi-detached binary system (see Bode & Evans 2008; Saikia & Anupama 2012; Woudt & Riberio 2014; Starrfield, Iliadis & Hicks 2016, for recent comprehensive reviews).

Following the explosion, some $10^{-5} - 10^{-4}$ M$_\odot$ of material, enriched in metals, is expelled at speeds of $\sim$ several hundred to $\sim$ several thousand km s^{-1}. CN explosions may occur on carbon-oxygen (CO) or oxygen-neon (ONe) WDs. The latter give rise to "fast" novae (see Payne-Gaposchkin 1957; Warner 2008, for a definition of CN speed class) that are characterised by coronal emission, the prodution of little or no dust, and are over-abundant (relative to solar abundances) in C, N, O, Ne, Mg, and Al; they are likely major producers of ^{22}Ne and ^{26}Al (Helton et al. 2012). On the other hand CNe originating on CO WDs tend to be "slow" or

⋆ E-mail: a.evans@keele.ac.uk

"moderate-speed" CNe, and often produce copious amounts of dust that is mainly carbonaceous.

Consequently, by ejecting gas and dust into the interstellar medium, CNe partake in the chemical enrichment of the Galaxy and indeed, there is evidence that nova debris was present when the Solar Nebula formed (Pepin et al. 2011; Haenecour et al. 2016).

Here we present ground-based infrared (IR) observations of the CN V339 Del (Nova Delphini 2013); observations of this CN from the *Stratospheric Observatory For Infrared Astronomy* (SOFIA; Young et al. 2012), together with near-contemporaneous photometry and spectroscopy obtained at the Mt Abu Infrared Observatory, India, and photometry from the O'Brien Observatory in Marine on St Croix, Minnesota, USA, have been described by Gehrz et al. (2015). IR observations of CNe are reviewed by Gehrz (2008), Banerjee & Ashok (2012), Evans & Gehrz (2012) and Gehrz, Evans & Woodward (2014). We also present an optical spectrum obtained at the Multiple Mirror Telescope (MMT), located on Mt Hopkins, Arizona.

2 V339 DELPHINI

V339 Del (PNV J20233073+2046041) was discovered – as a naked-eye nova – by Koichi Itagaki on 2013 August 14.584 UT (JD 2456519.084; Nakano et al. 2013), and spectroscopically confirmed by Darnley et al. (2013). Pre-outburst optical photometry showed that it was varying by a few tenths of a magnitude, around $\sim$ 17.5 magnitude, up to about 10 days before eruption (Deacon et al. 2014). Extensive broadband optical photometry following the eruption was given by Munari et al. (2013b). The visual light curve is given in Fig. 1(a). Munari et al. (2013a) determined the interstellar reddening to V339 Del to be $E(B-V) = 0.18$, which we adopt here.

Schaefer et al. (2014) obtained near-IR interferometry of V339 Del, measuring its angular size within a day of the eruption. They observed the expansion of the remnant and, in conjunction with an assumed ejection velocity of $613 \pm 79\,\mathrm{km\,s^{-1}}$, deduced a distance of 4.54 ± 0.59 kpc for the nova. They further detected an ellipticity in the light distribution, suggesting a prolate or bipolar structure that may have developed as early as day 2. On the basis of photometry of the expanding fireball following outburst, Gehrz et al. (2015) determined that the distance of V339 Del is 4.5 ± 0.8 kpc, and that the eruption occurred on 2013 August 13.9 UT (JD 2,456,518.4); in this paper we adopt this as $t = 0$ and $D = 4.5$ kpc.

Extensive optical spectroscopy during the early phase was described by Skopal et al. (2014). They determined that the effective temperature of the stellar remnant was in the range 6000–12000 K, and that the stellar remnant was super-Eddington. They determined the ejected mass to be a few $\times 10^{-4}\,\mathrm{M}_\odot$. Skopal et al. also reported the emergence of Raman-scattered O VI $\lambda = 1032, 1038$Å at around 6825Å (but see Shore et al. 2014, for a more plausible counter-interpretation in terms of emission by C I). Shore et al. (2016) have undertaken a multi-wavelength study of V339 Del, including X-ray data obtained with *Swift*, UV with the *Hubble Space Telescope*, and ground-based optical observations. The approximate duration of the X-ray phase, such that the X-ray count rate is at least 10% of the maximum count rate (see Figure 1 of Shore et al.), is indicated in Fig. 1.

Tarasova & Skopal (2014) presented optical spectra of V339 Del at resolution $\sim$ 1000. On the basis of Hα line profiles they concluded that the ejected material has a disc-polar structure,

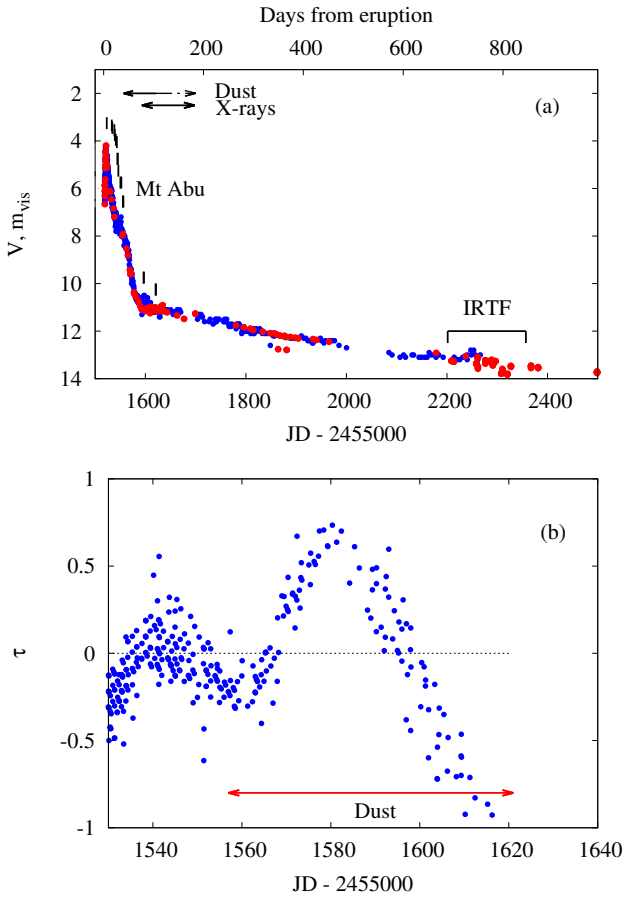

Figure 1. (a) Visual light curve of V339 Del. Blue, visual observations; red, CCD V-band observations. Times of the infrared observations discussed in this paper are indicated by vertical tick marks, as are the approximate durations of the dust and X-ray phases; the former is from infrared observaitons reported in this paper, the latter is the duration of the SSS phase from Shore et al. (2016). (b) Visual light curve, rectified by linear decline immediately before the onset of dust formation, showing dust optical depth. The extent of the dust phase is from (a). The apparent decline in τ for JD $-$ 2 455 000 $\gtrsim$ 1 600 is due to the increasing contribution of emission lines to the visual light. Note that the horizontal scales are diffent in (a) and (b). See text for discussion. Light curve data courtesy of the BAA and The Astronomer magazine.

with the orbital plane of the binary inclined at $\sim 65°$. They also estimated some elemental abundances and find that helium, neon and iron are close to solar, while nitrogen and oxygen are overabundant relative to solar by factors of 120 ± 60 and 8 ± 1.6 respectively. The mass of the ejecta, over the period 253 – 382 days after visual maximum, was estimated to be $\sim 7 \times 10^{-5}\,\mathrm{M}_\odot$.

V339 Del was observed with *Swift* (Kuulkers et al. 2013; Page et al. 2013a) shortly after outburst; no X-ray source was detected at the position of the nova which, however, was detected in all three ultra-violet (UV) filters of the UVOT instrument. The nova was weakly detected with *Swift* 30 days after the eruption (Page & Beardmore 2013); the emission at this time was consistent with shocked gas in the expanding shell, with no evidence for the super-soft source (SSS) X-ray emission commonly seen in CNe (see e.g. Krautter 2008). SSS emission was later detected, 55 days after the eruption (Page et al. 2013b). Quasi-Periodic Oscillations in the X-ray emission were reported by

Table 1. IR spectroscopic observing log for V339 Del.

Facility	Date UT YYYY-MM-DD	2013/15 UT Day	JD − 2450000	t (days)	Bands covered
Mt Abu	2013-08-18	Aug 18.63	6523.13	4.73	*JH*
Mt Abu	2013-08-28	Aug 28.66	6533.16	14.76	*JHK*
Mt Abu	2013-08-29	Aug 29.69	6534.19	15.79	*JHK*
Mt Abu	2013-09-02	Sep 02.68	6538.18	19.78	*JHK*
Mt Abu	2013-09-03	Sep 03.63	6539.13	20.73	*JK*
Mt Abu	2013-09-05	Sep 05.63	6541.13	22.73	*JHK*
Mt Abu	2013-09-07	Sep 07.62	6543.12	24.72	*JHK*
Mt Abu	2013-09-08	Sep 08.65	6544.15	25.75	*JHK*
Mt Abu	2013-09-09	Sep 09.60	6545.10	26.70	*JHK*
Mt Abu	2013-09-10	Sep 10.66	6546.16	27.76	*JHK*
Mt Abu	2013-09-14	Sep 14.72	6550.22	31.82	*JHK*
Mt Abu	2013-09-16	Sep 16.65	6552.15	33.75	*JHK*
Mt Abu	2013-09-19	Sep 19.72	6555.22	36.82	*JHK*
Mt Abu	2013-09-20	Sep 20.59	6556.09	37.69	*JHK*
Mt Abu	2013-10-30	Oct 30.69	6596.19	77.79	*JHK*
Mt Abu	2013-10-31	Oct 31.61	6597.11	78.71	*J*
Mt Abu	2013-11-23	Nov 23.62	6620.12	101.72	*J*
Mt Abu	2013-11-24	Nov 24.56	6621.06	102.66	*JHK*
IRTF	2015-06-28	Jun 28.41	7201.91	683.06	*IJHK*
IRTF	2015-12-01	Dec 1.21	7357.70	839.30	*IJHK*

Beardmore, Osborne & Page (2013) and Ness et al. (2013). A summary of the X-ray evolution is given by Shore et al. (2016).

V339 Del is one of an increasing number of CNe that have been detected as γ-ray sources (Hays et al. 2013; Ackermann et al. 2014; Ahnen et al. 2015); the peak in the γ-ray flux in V339 Del occurred about 6 days after optical maximum. In general, the γ-ray emission is thought to originate from the interaction between the nova ejecta with a pre-existing red-giant wind (e.g. Tatischeff & Hernanz 2007; Martin & Dubus 2013). However, V339 Del is one of only a handful of novae detected at γ-ray energies in which the donor is a main-sequence star, and therefore a different interpretation for the origin of the γ-ray emission is required (Ackermann et al. 2014). The first γ-ray detected nova with a main-sequence star, V595 Monocerotis, provided a vital clue in the bipolar morphology of the ejecta (Shore et al. 2013; Ribeiro, Munari & Valisa 2013; Linford et al. 2015). The bipolar morphology was interpreted as originating from the interaction of the ejecta with the motion of the binary system, allowing gas to be expelled freely in the polar directions, while within the equatorial plane material flowed more slowly; this set up a system of shocks, observed as synchrotron emission at radio frequencies, at the interface between the equatorial and polar regions where the γ-ray production was proposed to occur (Chomiuk et al. 2014).

IR photometric observations of V339 Del were reported by Cass et al. (2013a,b), Shenavrin et al (2013), Taranova et al. (2014) and Gehrz et al. (2015). Taranova et al. (2014) detected an IR excess due to dust formation approximately one month after maximum. They estimated a dust temperature and mass of $\sim$ 1500 K and $\sim 1.6 \times 10^{24}$ g ($\sim 8 \times 10^{-10}\,\mathrm{M}_\odot$) respectively on 2013 September 21 (day 38.9), and $\sim$ 1200 K and $\sim 10^{25}$ g ($\sim 5 \times 10^{-6}\,\mathrm{M}_\odot$) on 2013 October 11 (day 58.8). The presence of dust is confirmed by the IR photometry by Cass et al. (2013a) and Gehrz et al. (2015). Gehrz et al. estimated the amount of dust to be $\sim 1.3 \times 10^{-9}\,\mathrm{M}_\odot$ 78.66 days after outburst, and $\sim 1.2\ [\pm 0.4] \times 10^{-7}\,\mathrm{M}_\odot$ 102 days after outburst. Skopal et al. (2014) determined that the dust was located beyond the neutral hydrogen zone, where it was shielded from the hard radiation field of the stellar remnant (see e.g. Evans & Rawlings 1994; Williams et al. 2013).

IR spectroscopy of V339 Del was reported by Stringfellow, Hebb & Fumagalli (2013) and Banerjee et al. (2013a,b). These authors reported the presence of H I recombination lines, together with He I, O I and C I emission lines, the spectral evolution being typical of the taxonomic "Fe II class" of CNe (see Williams 1992, for a definition of the various CN spectral classes). The eruption most likely occurred on the surface of a CO white dwarf; such "CO novae" are often copious producers of dust. However, first overtone emission by CO, a common precursor to dust formation in CNe (e.g. Evans et al. 1996; Rudy et al. 2003; Das et al. 2009; Raj et al 2012; Banerjee et al. 2016), was not detected in any of these observations. It would have been detected had it been present to the extent seen in other novae; its weakness in V339 Del may be connected with this nova's inability to form a copious amount of dust.

Gehrz et al. (2015) have described IR observations of V339 Del using *SOFIA* and, using their fireball-derived distance, deduced an outburst luminosity of $\sim 8.3 \times 10^5\,\mathrm{L}_\odot$: V339 Del seems to have been the most luminous CO nova on record. They determined the mass of ejected gas to be $\sim 7.5 \times 10^{-5}\,\mathrm{M}_\odot$, and that the gas-to-dust ratio in V339 Del was in the range $\sim 470-940$. This implies that dust formation in V339 Del was much less efficient than is the case for other CO novae. The inefficient dust formation in V339 Del may be connected to the weak or absent CO first overtone emission.

3 OBSERVATIONS

IR spectroscopy of V339 Del was obtained at Mt Abu and at the 3 m NASA Infrared Telescope Facility (IRTF; Becklin & Capps 1981); a summary of the observations obtained is given in Table 1, in which t is the time from the nova explosion reckoned from the $t = 0$ date given in Section 2.

3.1 Mount Abu

IR photometry in the *JHK* bands, and $1 - 2.5\,\mu$m spectroscopy, of V339 Del were obtained with the 1.2 m telescope of the Mt Abu Infrared Observatory (see e.g. Banerjee & Ashok 2012) over the period 2013 August 18 – 2013 November 11. IR photometry of V339 Del obtained at Mt Abu is included in Table 4 of Gehrz et al. (2015), which also gives full details of the observing and data reduction procedures; the photometric data and these details are not repeated here. The spectra are shown in Fig. 2.

3.2 IRTF

Two spectra, covering the 0.78 – 2.5 μm region, were obtained on 2015 June 28.409 UT and 2015 December 1.20 UT using the 3 m NASA IRTF. The integration times for these spectra were 1497 s and 2395 s respectively. The spectra were obtained using SpeX (Rayner et al. 2003) in the cross-dispersed mode using the $0.5'' \times 15''$ slit at a resolution of $R = 2000$. Data reduction and calibration was done using the SPEXTOOL software (Cushing, Vacca & Rayner 2004) with corrections for telluric absorption being performed using the IDL tool XTELLCOR (Vacca et al. 2003). The IRTF spectra are shown in Fig. 3.

The IRTF spectrum obtained on day 683.06 is also shown with line identifications in Fig. 3. The spectrum shows a number of

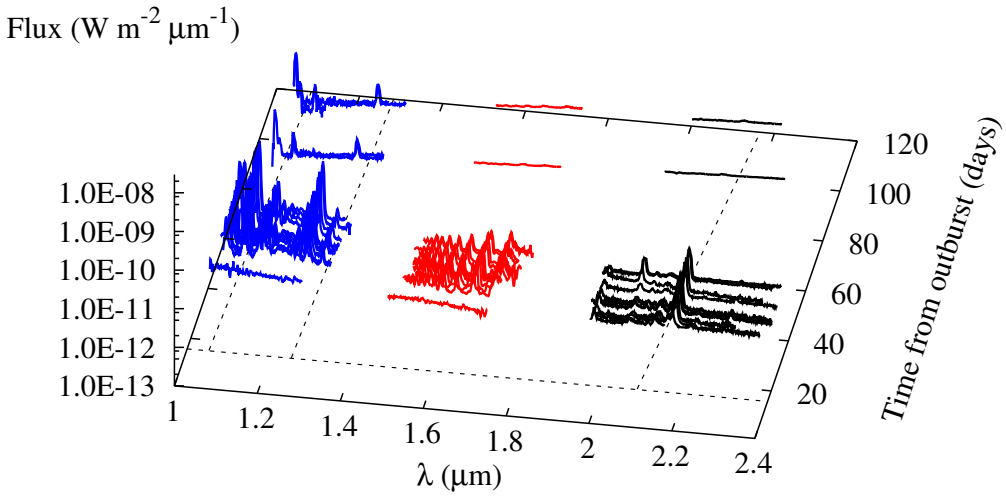

Figure 2. Evolution of the *JHK* spectrum as seen from Mt Abu. Blue curves: J-band data; red curves: H-band data; black curves: K-band data. Dashed lines delineate He I 1.0833 μm, Paβ 1.2821 μm, Brγ 2.1662 μm. The transition from gas emission, with the flux declining to longer wavelengths ($t < 40$ days), to gas+dust emission, with flux rising to longer wavelengths ($t > 77$ days), is evident. The dashed line at $t = 15.79$ days indicates an approximate baseline for the 15.79 day data, to give an indication of the flux scale.

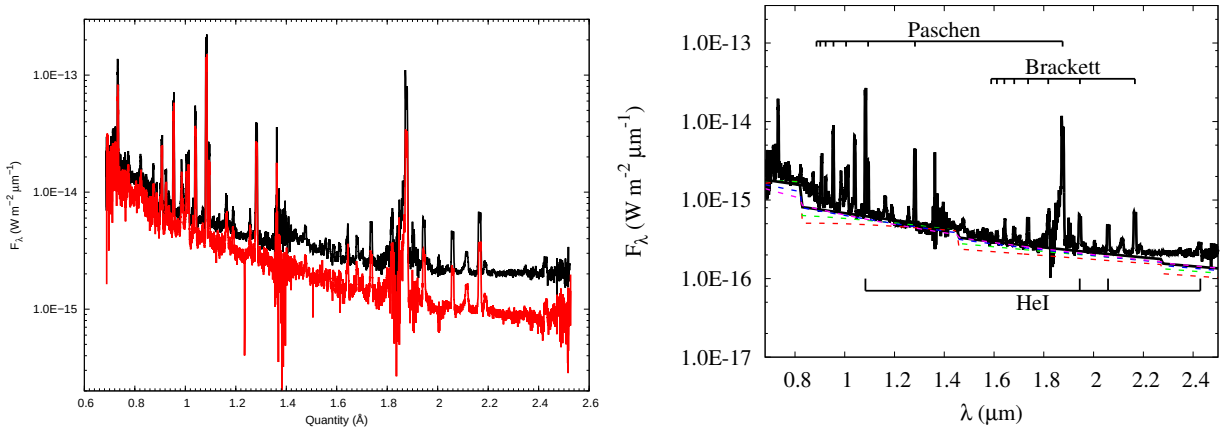

Figure 3. Left: IR spectra of V339 Del obtained at the IRTF; black spectrum obtained on 2015 Jun 28.46 (day 683.06), red spectrum on 2015 Dec 1.21 (day 839.30). Right: Spectrum obtained on the IRTF on 2015 June 28.46, with prominent emission lines identified. The dotted curves are free-free and free-bound emission by a gas having electron temperature 4×10^4 K (magenta), 2×10^4 K (blue), 10^4 K (green) and 8×10^3 K (red). The solid black curve is the best fit for free-free emission with electron temperature 1.5×10^4 K. Note the weak dust excess at wavelengths $\gtrsim 2\,\mu$m. See text for details.

prominent emission lines, primarily hydrogen and He II recombination lines and He I. The emission lines show a castellated structure that is present in both hydrogen and helium lines.

In both the Mt Abu and IRTF data the emission lines sit atop a nebular continuum. We determine the nebular continuum using an assumed flux for the Balmer Hβ line, and an electron temperature and density. We have calculated several nebular continua using NEBCONT, which is part of the STARLINK (Currie et al. 2014) DIPSO spectral analysis package (Howarth et al. 2004). NEBCONT includes free-bound continua from H, He, CNO and Ne, as well as the 2s–1s 2-photon continuum from H and He II. DIPSO requires electron temperature and density and the Hβ flux (amongst other parameters) as input.

For n_e we extrapolate the value in Gehrz et al. (2015) for day 3.25, namely $n_e = 10^{13}$ cm^{-3}; Gehrz et al. argue that the electron density declines with time as $n_e \propto t^{-2}$, giving $n_e =$

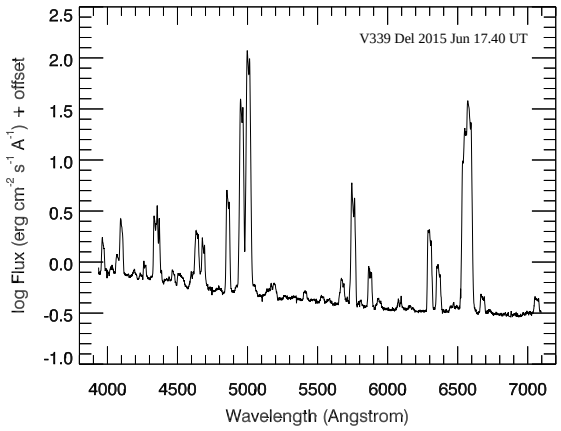

Figure 4. Optical spectrum of V339 Del obtained at the MMT Observatory (2015 June 17.40 UT = day 672.50). The ordinate is log of the observed flux plus an offset (= 14.0) to reveal details of the individual line profiles. The spectrum of V339 Del at this epoch is similar to other classical novae in the nebular phase (Williams 2012), exhibiting emission lines of the Balmer series of H, He I and He II, [N II], C II, [O I] and [O III], coinciding with the decline of emission from various Fe multiplet transitions. The emission line profiles of both H and metal ions exhibited a "double-horned" structure across the line peaks. A complete identification of spectral lines present in the this spectrum are detailed in Table A3 in Appendix A.

2.26×10^8 cm^{-3} at the time of the 2015 June IRTF observation ($t = 683.06$ days). This is substantially higher than the value ($\sim 4 \times 10^5$ cm^{-3}) deduced by Shore et al. (2016) as early as day 435. There are two reasons for this: First we note that Shore et al. used the [O III]5007+4959/[O III]4363 flux ratio to determine n_e; the 5007, 4959Å lines have a critical density for collisional de-excitation of 6.8×10^5 cm^{-3} at $T_e = 10^4$ K (Osterbrock & Ferland 2006). Since the H recombination line fluxes are $\propto {n_e}^2$, the H I emission must come primarily from high density regions, with minimal contribution from low density regions in which [O III] emission originates. Indeed the [O III]5007+4959/[O III]4363 flux ratio in Fig. 4, obtained at about the same time as the 2015 June IRTF spectrum, is $\simeq 67.3$, giving $n_e \simeq 4.8 \times 10^5$ cm^{-3}, consistent with Shore et al. (2016). And second, we have assumed $n_e \propto t^{-2}$ as opposed to the t^{-3} dependence assumed by Shore et al..

We explore T_e values in the range $0.8 - 4 \times 10^4$ K. To estimate the Hβ flux, a near-contemporaneous optical spectrum of V339 Del, taken by D. Boyd on 2015 July 5, was obtained from the *Astronomical Ring for Access to Spectroscopy* (ARAS) database[1]. This was flux calibrated by anchoring the V-band centre using $V = 13.3 \pm 0.2$ magnitudes. Using IRAF[2], the measured Hβ flux was found to be $(2.0 \pm 0.4) \times 10^{-15}$ W m^{-2}; dereddening by $E(B-V) = 0.18$ leads to a dereddened Hβ flux of $\sim 3.5 \times 10^{-15}$ W m^2. We use this as a guide to fit the nebular continuum and we vary the Hβ flux to get a reasonable fit (by eye) to the *JHK* data. We used $T_e = 4 \times 10^4$ K, Hβ flux 1.86×10^{-15} W m^{-2}; $T_e = 2 \times 10^4$K, 2.82×10^{-15} W m^{-2}; $T_e = 1 \times 10^4$K, 2.07×10^{-15} W m^{-2}; $T_e = 8 \times 10^3$K, 2.07×10^{-15} W m^{-2}; and $T_e = 1.5 \times 10^4$K, 3.63×10^{-15} W m^{-2}. The uncertainties in the Hβ fluxes are typically ± 0.1 dex.

The observed magnitude of the Paschen discontinuity at the 0.820 μm limit, and of the Brackett discontinuity at 1.459 μm, show that T_e must lie between 10^4 K and 4×10^4 K; the calculated continuum for 1.5×10^4 K seems to give a reasonable fit to the continuum, but 2×10^4 K provides a better fit to the magnitude of the discontinuities. Where necessary we assume the latter value in what follows.

It is evident in Fig. 3 that there is a weak excess longward of ~ 2 μm on day 683.06; this is residual emission due to dust, which was far more prominent in the early evolution of V339 Del (see Section 5 below).

3.3 MMT

An optical spectrum of V339 Del was obtained on 2015 June 17.40 UT (day 672.50) at the 6.5 m MMT with the Blue Channel Spectrograph (Schmidt et al. 1989). A $1'' \times 180''$ long–slit was used with a 500 line per mm grating and a thinned STA 2688×512 pixel detector covering all or part of the 3800–7100 Å region at a nominal resolution of 3.6 Å. A UV–36 long–pass filter was used to block 2nd order light from contaminating the red portion of our spectra. Spectra of a HeArNe lamp provided wavelength calibration while the spectra of a quartz–halogen lamp provided flatfield correction images. Twenty, individual 10-s exposure spectra were extracted and coadded to produce the final spectrum, which is shown in Fig. 4. The spectrophotometric standard star Kopff 27 was obtained to provide flux calibration.

The data were reduced using standard IRAF packages and standard spectral extraction and calibration techniques were used.

4 THE EMISSION LINES AND NEBULAR CONTINUUM

4.1 Emission lines and line fluxes

The spectra of V339 Del in the $1 - 2.5$ μm region, taken from Mt Abu, are shown in a compact fashion in Fig. 2; an expanded view of representative spectra, where individual lines are more clearly visible, is shown in Fig. 7, which is further discussed below. Among the emission lines seen during the early phase are prominent lines of hydrogen from the Paschen and Brackett series (viz. Pa 5–3, 6–3, Br 7–4 and Br 10–4 through Br 17–4). Helium lines are weak during this stage but increase in strength later; the main lines seen are He I 1.0833 μm, 2.0581 μm. N I lines are few, the strongest N I feature being the 1.2461/1.2469 μm line. In addition, there is a cluster of weaker N I features, blended with many C I lines, lying between 1.2 and 1.275 μm. The most prominent O I lines are the Lyβ fluoresced 1.1287 μm line, which is one of the strongest lines in the spectrum, and the relatively weaker, continuum excited O I 1.3164 μm line. A large number of prominent carbon lines are seen which include C I lines at 1.165, 1.175, 1.188, 1.689 μm, as well as the forest of strong C I lines between 1.74—1.8 μm at the H-band edge. As discussed in Banerjee & Ashok (2012), these C I lines are the easiest way to demarcate the Fe II from the He/N class of novae in the near-IR. In brief, the near-IR spectra of V339 Del are typical of the IR properties of the Fe II class of novae. Several examples of the near-IR spectra of novae of this class, such as V1280 Sco, V2615 Oph, V476 Sct, etc., are given in Banerjee & Ashok and references therein. A detailed identification of the lines seen in the

[1] http://www.astrosurf.com/aras/Aras_DataBase/Novae
[2] IRAF is distributed by the National Optical Astronomy Observatories, which are operated by the Association of Universities for Research in Astronomy, Inc., under cooperative agreement with the National Science Foundation.

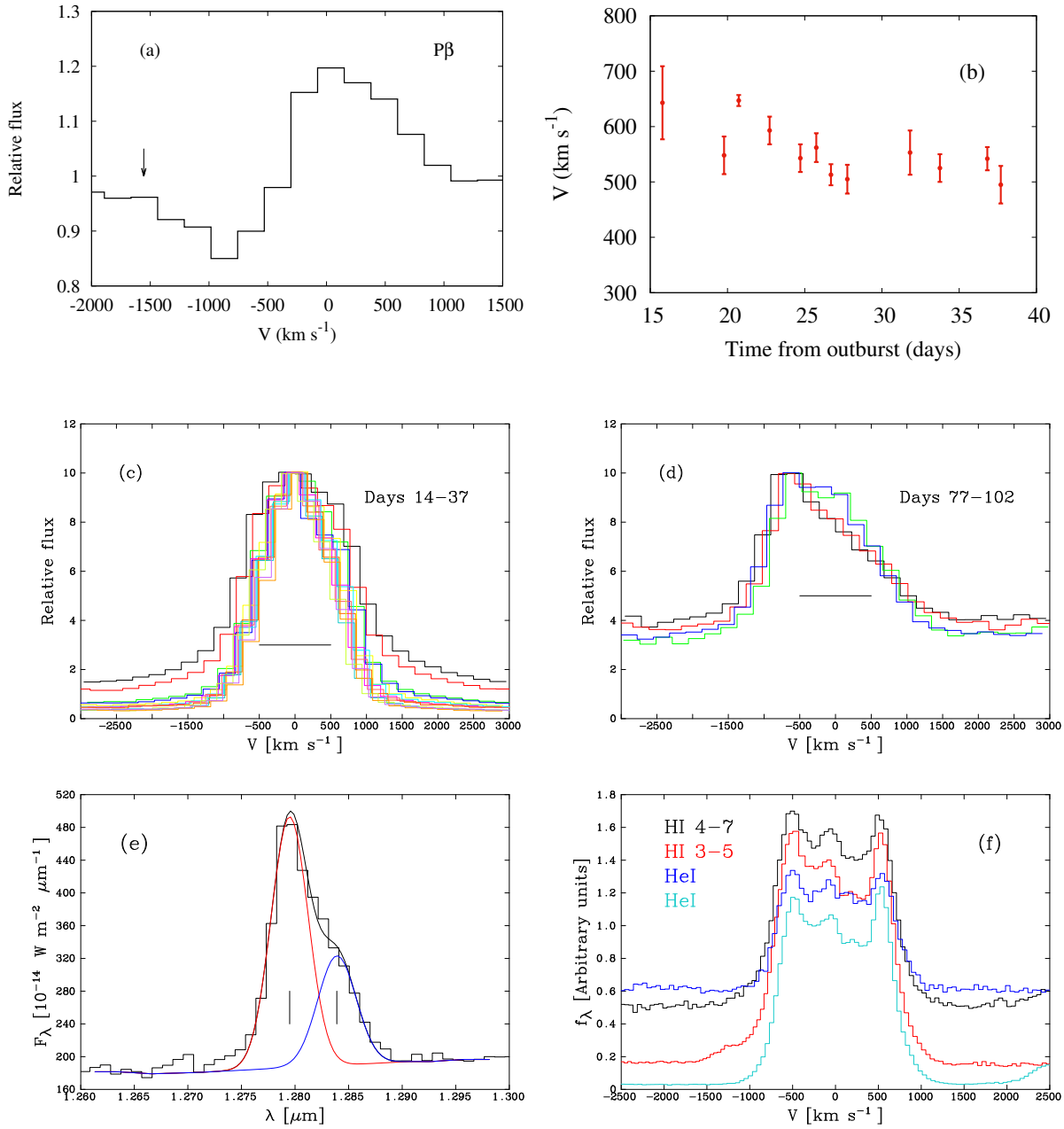

Figure 5. (a) P Cygni profile in Paβ on day $t = 4.73$ days. (b) Expansion velocity as deduced from IR H I recombination lines over the period 14 – 37 days. (c) Spectrum around 1.282 μm Paβ line over the period 14 – 37 days. (d) Spectrum around 1.282 μm Paβ line over the period 77 – 102 days. The black horizontal lines in (c) and (d) delineate $\pm 500\,\mathrm{km\,s^{-1}}$. (e) Profile of the Pa$\beta$ line on day 77.79; vertical lines are at the central wavelength of the two components, at 1.2795 μm and 1.2839 μm; the corresponding Gaussian profiles (red and blue) and the overall profile (black) are also shown. (f) Line profiles in velocity space on day 683.06 for H I Brγ (4–7; black), H I Pβ (3–5; red), He I ^{3}S$-^3$P$_o$ (1.083 μm; dark blue) and He I ^{1}S$-^1$P$_o$ (2.059 μm; light blue).

spectra of V339 Del, along with line fluxes – uncorrected for extinction – are listed in Tables A1 and A2 in Appendix A.

4.2 Expansion velocities

On day 4.73 there is a clear P Cygni profile in the Paβ line (see Fig. 5(a)), with a suggested terminal velocity of $\sim -1\,500\,\mathrm{km\,s^{-1}}$; a P Cygni profile with similar terminal velocity is also present in the C I ^{3}P$_2-^3$P$_2^o$ line at 1.2717 μm. These were no longer present by day 14.76. In the optical, Skopal et al. (2014) found that the Hα line displayed a P-Cyg profile, with terminal velocity $-1\,600\,\mathrm{km\,s^{-1}}$ at $t \simeq 0.95$ day, decreasing to $-730\,\mathrm{km\,s^{-1}}$ at $t \simeq 6$ days. Despite the lower resolution of our IR data at this time, the IR terminal velocity seems consistent with that in the optical.

The Half Width Half Maximum (HWHM) of the emission lines can be used to estimate the expansion velocity V of the ejecta. While the Full Width at Zero Intensity (FWZI) captures high velocity wings (see Fig. 5(c),(d),(f) below) the HWHM better characterises the bulk of the ejecta. In Fig. 5(b) we show the dependence of the HWHM velocities (corrected for instrumental resolution) on time t since outburst. There may be a decline in V over the period $t = 14 - 37$ days (see Fig. 5(b)) but this is marginal at best. The

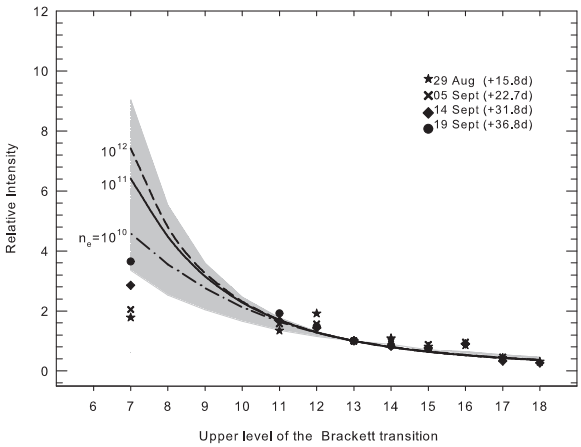

Figure 6. The relative intensities of the Brackett lines, with Br-13 set to unity, for four early epochs of the Mt Abu observations (viz. 2013 Aug 29, Sept 5, 15 and 19). The parameter space for the predicted Case B values is shown in grey for combinations of electron density and temperature varying between 10^5 to 10^{14} cm^{-3}, and $T_e = 5\,000$ to $20\,000$ K respectively. Three specific Case B curves are shown, for $T = 10\,000$ K and $n_e = 10^{10}, 10^{11}$ and 10^{12} cm^{-3} (dash-dot, dashed and continuous curves respectively). Such high densities are expected in the ejecta during the early evolution.

weighted mean of the velocites in Fig. 5(b) is $583\,\mathrm{km\,s^{-1}}$ and we assume this value in what follows.

From $t \simeq 77$ days, however, there seems to have been a significant change in the profile of the Paβ line (Fig. 5(c)-(d)). Prior to day 37 Paβ is symmetrical, with HWHM $\simeq 530\,\mathrm{km\,s^{-1}}$ but by day 77, there is a distinct asymmetry. A simple Gaussian fit to the Paβ line for day 77.79 shows evidence for two distinct features, with HWHM velocites of $418\,\mathrm{km\,s^{-1}}$ (blue component) and $437\,\mathrm{km\,s^{-1}}$ (red component), deconvolved for the instrumental resolution. The line centroids are at velocities of $-622\,\mathrm{km\,s^{-1}}$ and $+407\,\mathrm{km\,s^{-1}}$, respectively (Fig. 5(e)). This change in profile coindides with the epoch of maximum dust mass (see Section 5). The data presented here suggest that the torus was obscuring the receding lobe as early as day 77. By day 683.06, however, the blue wing seems to have recovered (see Fig. 5(f)), possibly due to dispersal of the dust or, more likely, due to the destruction of a large fraction of the dust shell (see Section 5.4 below).

4.3 Case B analysis

A recombination Case B analysis was carried out for four epochs (Fig. 6) between 15.8 to 36.8 d after outburst, before dust formation set in. The analysis was along similar lines as for Nova Cep 2014 (Srivastava et al. 2015). Fig.6 shows the Brackett line strengths with respect to Br13 set to unity. The line fluxes do not match predicted Case B values and the Brγ line strength is significantly lower than the values predicted by Storey & Hummer (1995). This indicates that Brγ is optically thick, and so possibly are the other Br lines. Similar optical depth effects in the Br lines, due to high plasma densities during the early stages after outburst, is common and has been seen in several other novae e.g. Nova Oph 1998 (Lynch et al. 2000), V2491 Cyg, V597 Pup, RS Oph, T Pyx, Nova Cep 2014 (see Naik et al. 2009; Joshi et al. 2014; Srivastava et al. 2015, and references therein).

Following the formalism of Hummer & Storey (1987) and Storey & Hummer (1995), the optical depth at the Brγ line-center is given by

$$\tau_{n,n'} = n_e\, n_i\, \Omega(n,n')\, R \ ,$$

where n_e and n_i are the electron and ion densities respectively, which are assumed to be equal, and $\Omega(n,n')$ is the opacity corresponding to the transition from upper level n to lower level n', values of which are listed in Storey & Hummer (1995). The path length R is taken as the kinematical distance $R = Vt$ travelled by the ejecta, where $V = 583\,\mathrm{km\,s^{-1}}$ is the velocity of ejecta and t is the time after outburst. We consider values of t between 15.8 day to 36.8 day (from Fig. 6) and set the constraint that $\tau(\mathrm{Br}\gamma) = n_e n_i \Omega(n,n') R$ be greater than 1. The lower limit on the electron density n_e is then found to be in the range 0.41×10^{10} cm^{-3} to 0.98×10^{10} cm^{-3} on day 15.8. By day 36.8, the density decreases in the range 0.27×10^{10} cm^{-3} to 0.64×10^{10} cm^{-3}. These derived lower limits should be smaller than the actual n_e values because $\tau(\mathrm{Br}\gamma)$ can be considerably > 1. An additional caveat in this analysis is the intrinsic assumption of spherical geometry for the ejecta. (Slavin, O'Brien & Dunlop 1995) since a bipolar morphology appears more appropriate for V339 Del (see also Schaefer et al. 2014; Shore et al. 2016).

A rough estimate of the ejected mass may be obtained using

$$M_{ej} = \phi\, V n_e m_H \ ,$$

where $V (= 4/3\pi R^3)$ is the volume, ϕ is the volume filling factor (assumed $= 0.1$ from Shore et al. 2016) and m_H is the proton mass. We use the lower limits on n_e estimated above and allow R to vary between the distance traversed from 15.8 d to 36.8 d. The lower limit on the mass M_{ej} is estimated to lie between 0.05×10^{-5} to $0.17 \times 10^{-5}\,\mathrm{M_\odot}$. These estimates are roughly a factor of 10 – 20 times lower than the mass estimates given by Gehrz et al. (2015) and Shore et al. (2016), which lie in the range $(1-3) \times 10^{-5}\,\mathrm{M_\odot}$, but as noted above our values are lower limits.

4.4 Optical Spectra

By day 672 V339 Del had evolved into the nebular phase of its evolution. Our optical spectroscopy (Fig. 4) show at this epoch emission was dominated by recombination lines from the hydrogen Balmer series, helium ions and low ionization, forbidden line emission from metals such as C, N, O, Si, and Fe. The strongest emission lines in the spectra arise from [O III]4958.91/5006.84 Å. The peak of the emission line profiles exhibit a "double-horn" structure indicating that the total observed emission at a given wavelength arises from material receding from and approaching the observer (i.e., a ring or shell structure to the ejecta).

Using the IRAF SPLOT deblending tool, the components of line profiles were deblended assuming a simple model for the ejecta geometry wherein two Gaussian components were fit to an emission line using the average value of the local continuum using a non-linear least squares technique. Fig. 8 shows the structure of the optical Balmer Hβ line with the two fit velocity components, which are similar to those seen in the infrared Paschen and Brackett series lines depicted in Fig. 5(f) observed on day 683.06. The spectral resolution of the optical and infrared spectra are comparable, and while the velocity peak of the blue shifted material is of the order -500 km s^{-1}, that of the red shifted material differs by $\simeq 100\,\mathrm{km\,s^{-1}}$ between the optical and the infrared profiles. However, this is less than the optical velocity resolution ($\approx 185\,\mathrm{km\,s^{-1}}$) hence we consider the two measurements comparable.

Emission from metal ions also dominates the optical spectra. The strongest of these lines also exhibit emission from two velocity

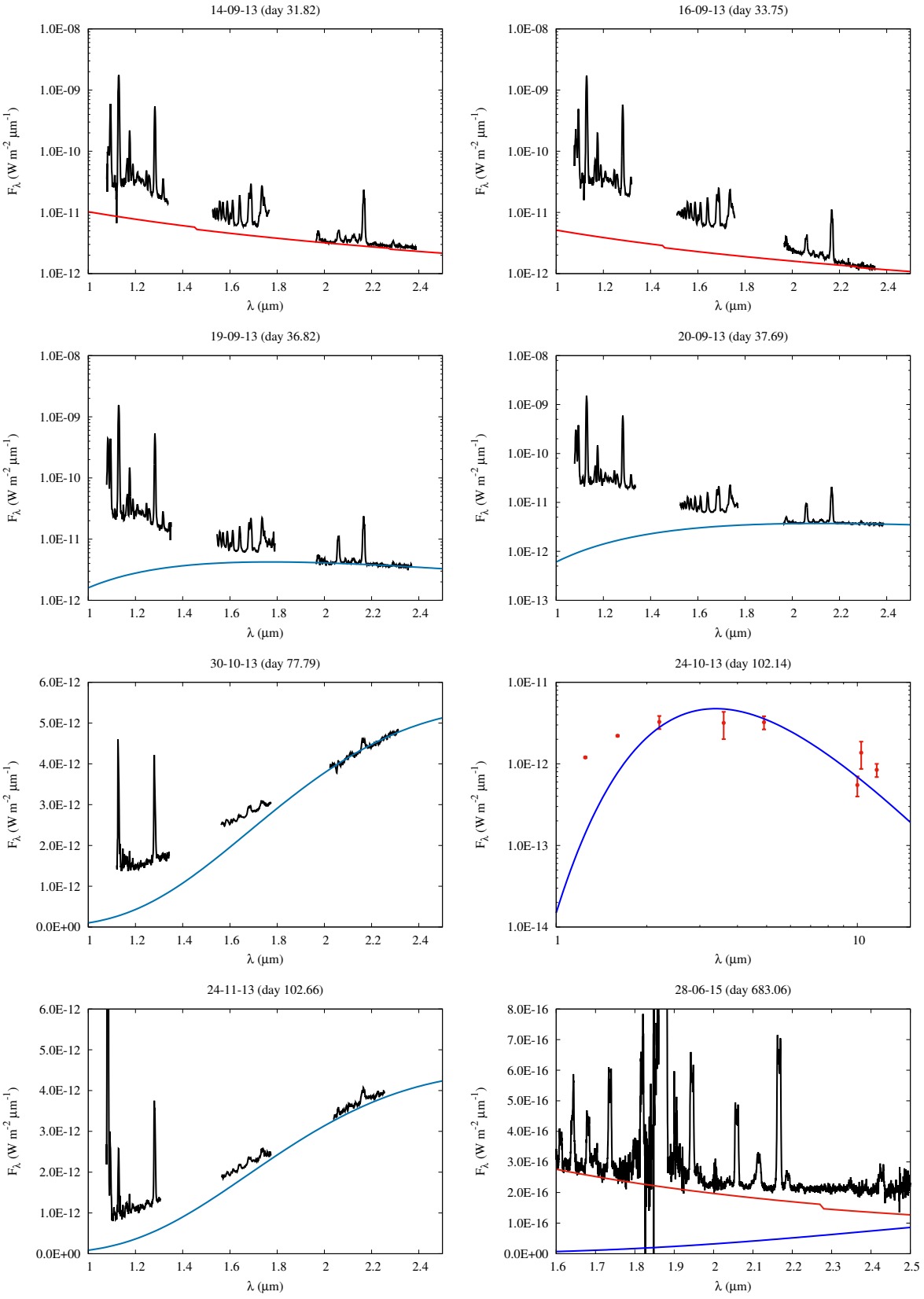

Figure 7. Evolution of the IR spectral energy distribution from day 31.82 to day 683.06. Data, shown as black lines, dereddened by $E(B-V) = 0.18$. Blue lines, black body function fitted to K-band data; red lines free-free and free-bound emission. The 2013 November 24 (day 102.14) plot shows the O'Brien Observatory photometry reported in Gehrz et al. (2015), dereddened by $E(B-V) = 0.18$. For the 2015 June 28 plot, the additional red curve is the contribution from free-free and free-bound emission. See text for details.

Table 2. Dust evolution in V339 Del. "BB" denotes black body grains, "AC" denotes amorphous carbon, "GR" denotes graphitic carbon. For the black body case, a grain radius $a = 1\,\mu$m is assumed.

t (days)	$[\lambda f_\lambda]_{\max}$ (10^{-12} W m^{-2})	$T_{\rm d}$ (K)	$M_{\rm d}$ (10^{-9} M$_\odot$)			$a(\mu$m)	
			BB	AC	GR	AC	GR
36.82	8.41 [±0.67]	1 637 ± 65	25.6 ± 0.58	1.66 ± 0.34	2.33 ± 0.52	2.97	4.29
37.69	8.85 [±1.38]	1 365 ± 44	55.8 ± 1.31	4.15 ± 0.91	6.44 ± 1.48	6.72	10.64
77.79	17.2 [±0.3]	1 014 ± 3	356 ± 0.7	33.1 ± 0.74	6.07 ± 1.42	6.46	11.93
102.14	2.59 [±1.02]	854 ± 74	107 ± 5.52	11.28 ± 6.40	22.79 ± 1.37	8.47	1.07
102.66	14.1 [±0.4]	1 017 ± 4	289 ± 0.93	26.76 ± 0.91	49.02 ± 1.72	3.66	6.74
683.06	2.93 [±] × 10^{-2}	684 ± ∼ 50	0.37[±0.16]	0.84[±0.0.41]	0.87[±0.42]	0.54	1.23

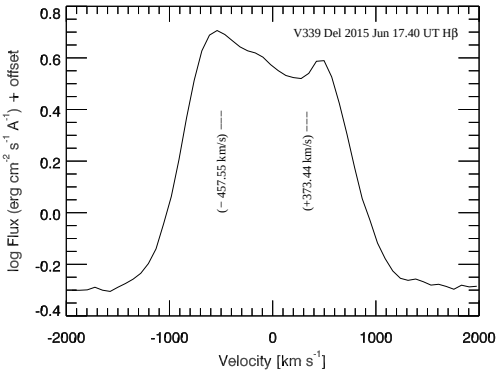

Figure 8. The Hβ line profile of V339 Del observed on 2015 June 17.40 UT, extracted from the spectra shown in Figure 4. Fitting a simple two-Gaussian model to deblend the velocity components of the Hβ profile reveals two peaks, one blue shifted by 457.55 km s^{-1} and one red shifted by 373.4 km s^{-1} from the rest wavelength of 4 861.33 Å (in air) for the transition, with Gaussian full width half maxima of 11.32 Å and 11.147 Å, respectively.

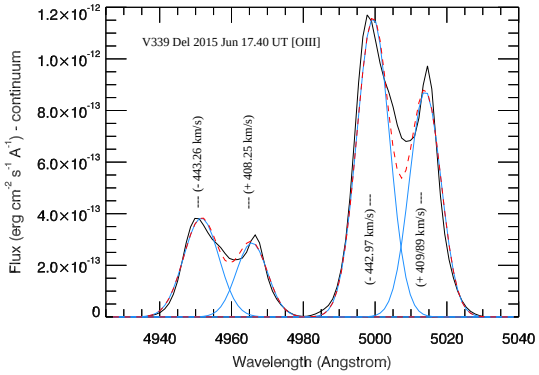

Figure 9. The [O III] line profiles of V339 Del observed on 2015 June 17.40 UT, extracted from the spectra shown in Fig. 4. The profile peaks exhibit the same structure as the Balmer series emission lines (Fig. 8). Fitting a simple two-Gaussian model to deblend the velocity components of these forbidden lines returns components for the 4958.91 / 5006.84 lines (wavelength in air) and Gaussian full width half maxima of -443.26 km s^{-1}, 11.55 Å; $+408.25$ km s^{-1}, 10.21 Å and -442.97 km s^{-1}, 11.71 Å; $+409.89$ km s^{-1}, 10.35 Å, respectively. The solid blue curves are the normalised Gaussian fits to each component, the dashed red line is the composite sum of the normalised Gaussian, and the solid black line is the original data.

components as seen in the Balmer lines. Fig. 9 shows the Gaussian deblending of the [O III]4958/5006 Å (rest wavelengths in air) forbidden line profiles with the velocity components marked as well as each Gaussian fit. The sum total of the two components are overlain on the observed emission profiles from the spectra for comparison. Various lines were fit using this technique with integrated line fluxes determined from measurements of the line cores and Gaussian full width half maxima. A detailed description of line identifications derived from the optical spectra on day 672.50 – uncorrected for extinction – is summarised in Table A3 in Appendix A.

Detailed use of the optical and infrared line fluxes observed over multiple epochs as input to photoionization abundance synthesis models is discussed in a forthcoming manuscript.

5 EVOLUTION OF THE DUST

The evolution of the IR spectral energy distribution is shown in Fig. 7. On some of the epochs there is a clear IR excess at the longer wavelengths, which we attribute to the dust reported by Shenavrin et al (2013) and Gehrz et al. (2015); it is also evident that there is a contribution from free-free and free-bound emission, although this becomes less important in the K-band. There is no evidence for the presence of dust on or before 2013 September 16 (day 33.75; see Fig. 7).

We attempted to fit a function of the form

$$f_\lambda = \frac{C}{\lambda^{(5+\beta)}} \frac{1}{\exp[hc/\lambda k T_{\rm d}] - 1}$$

to the excess. Here C is a scaling factor, β is the "β-index" for the dust, defined in the usual way such that the dust emisivity is $\propto \lambda^{-\beta}$, and $T_{\rm d}$ is the dust temperature. However, a non-zero value of β persistently gave a poor fit for all datasets; best fits were obtained by forcing $\beta \equiv 0$, i.e. pure black body emission by the dust shell, although this does not of course necessarily imply black body dust grains. The deduced black body temperatures are typically in the range $\sim 800 - 1600$ K. At these temperatures f_λ peaks around $1.8 - 2.8\,\mu$m and the K-band data alone are sufficient to pin down the temperature; this is particularly helpful as the free-free emission is (apart from the IRTF spectrum obtained on day 683.06) less prominent at these wavelengths. For example, fitting the black body function to both H- and K-band spectroscopic data for day 102.66 gives a dust temperature of 1 087±2 K, compared with 1 017±4 K for the K-band data alone (see Table 2); the formal temperature errors are small compared with T as a consequence of the large number of data points in the fit. In view of the uncertainties in the

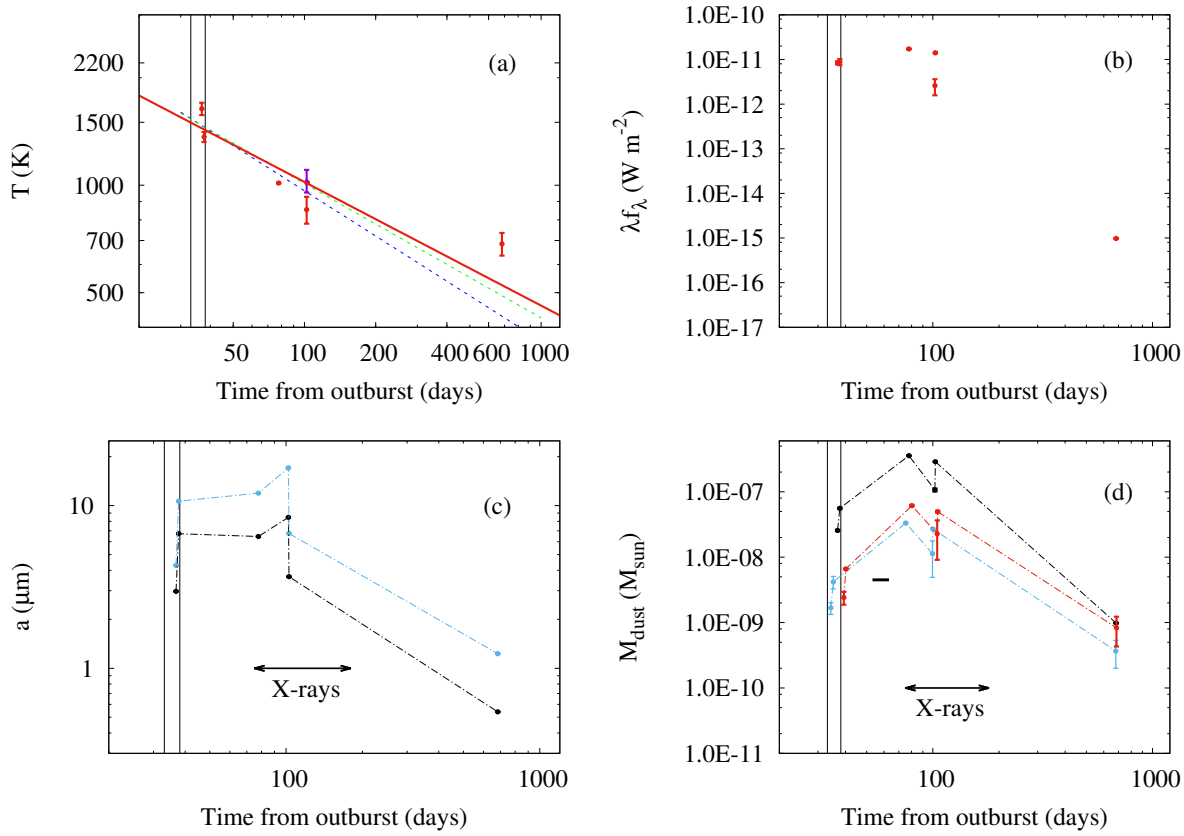

Figure 10. Evolution of the dust; in each panel the vertical lines denote constraints on the epoch of dust formation. (a) Dust temperature; the magenta point at $t = 102.14$ days is based on O'Brien Observatory photometry. The solid line is a fit of $T \propto t^{-\sigma}$. The broken green line is the expected relationship for graphitic carbon; the broken blue line is the expected relationship for amorphous carbon. (b) Dust flux, given by $\{\lambda f_\lambda\}_{\rm max}$. (c) Grain radius, for AC (black) and GR (blue) grains. (d) Dust mass, calculated for 1 μm black body grains (black points), amorphous carbon grains (blue points) and graphitic carbon grains (red points). The data for amorphous carbon and graphitic carbon have been offset by –2.5 days and +2.5 days respectively, for clarity, and dotted lines are included to guide the eye. The short horizontal line depicts the dust mass reported by Taranova et al. (2014). Uncertainties are smaller than the plotted points unless indicated. In panels (c) and (d) the approximate duration of the super-soft X-ray phase, from Fig. 1(a), is indicated. See text for details.

flux calibration and in fitting the grain parameters (see below) we do not consider the difference to be significant.

We have therefore fitted the K-band data – with emission lines removed – with black bodies; the fits are shown in Fig. 7. The evolution of the temperature and dust flux (as given by $\{\lambda f_\lambda\}_{\rm max}$) are listed in Table 2 and shown in Fig. 10(a) and (b) respectively. There is no clear evidence for the presence of dust on 2013 September 16 (day 33.75; see Fig. 7, top right panel); this is consistent with the conclusion of Taranova et al. (2014), who found that dust formation occurred around 2013 September 17. These authors determined a $(K - L)$ colour temperature of $\simeq$ 1500 K on 2013 September 21, and $\simeq$ 1200 K on 2013 October 11, close to the values reported in Table 2.

There remains a weak dust excess on day 683.06 but it is clear from Figs 3 and 7 that free-free and free-bound emission by the gas is comparable with, if not dominating, the dust emission by this time. We have removed the free-free and free-bound emission as determined in Section 3.2 to determine the dust excess, which has a black body temperature of 651 K. There is no trace of dust emission shortward of 2.5 μm by day 839.30.

5.1 The nature of the dust

To determine the nature of the dust, including dust mass and grain radius, we use the information in Appendix B; this includes a revised Planck Mean absorption efficiency for carbon dust, determined from the data in Blanco, Falcicchia & Merico (1983). The relevant information, including formulae, is given in Appendix B.

5.1.1 Grain radius

To determine grain radius we use Equation (6) of Gehrz et al. (2016), with $L_* = 8.3 \times 10^5\,{\rm L}_\odot$ and $R = Vt$, where $V = 583\,{\rm km\,s^{-1}}$ (see above).

The dependence of grain radius on time is shown in Fig. 10(c). In reality of course, there will be a distribution of grain sizes (see e.g. Evans et al. 2005) and the grain size calculated in this way gives an average over the dust shell. However, it seems clear that there is a rapid rise in the grain size immediately following grain formation, eventually followed by a phase in which the grain size diminishes substantially. This is further discussed below.

5.1.2 *Dust mass*

Black body grains. For black body (BB) grains the dust mass is given by (see Equation (B4))

$$\frac{M_{\rm d}}{\rm M_\odot} \simeq 2.19 \times 10^{15} \ \frac{\{\lambda f_\lambda\}_{\rm max}}{\rm W\ m^{-2}} \ \frac{1}{T_{\rm d}^4} \qquad (1)$$

where we have assumed 1 μm carbon grains ($\rho = 2.25$ g cm^{-3}) and distance $D = 4.5$ kpc. The dust masses are included in Table 2 in the column headed BB; the uncertainties have been propagated from the uncertainties in $\{\lambda f_\lambda\}_{\rm max}$ and $T_{\rm d}$. The dependence of dust mass on time is shown Fig. 10(d).

Optically thin amorphous carbon. For amorphous carbon (AC) grains (see Equation (B2))

$$\frac{M_{\rm dust}}{\rm M_\odot} \simeq 3.76 \times 10^{17} \ \frac{\{\lambda f_\lambda\}_{\rm max}}{T_{\rm d}^{4.754}}$$

where we have again taken $D = 4.5$ kpc and grain density 2.25 g cm^{-3} for carbon. The dust masses are again included in Table 2 (column AC) and shown in Fig. 10(d).

Optically thin graphitic carbon. For graphitic carbon (GC) grains (again see Equation (B2))

$$\frac{M_{\rm d}}{\rm M_\odot} \simeq 3.35 \times 10^{19} \ \frac{\{\lambda f_\lambda\}_{\rm max}}{T_{\rm d}^{5.315}}$$

for $D = 4.5$ kpc. The masses are given in Table 2 (column GR) and shown in Fig. 10(d). As with grain radius, there seems to be evidence for a rapid rise in dust mass, followed by a steep decline, irrespective of the composition of the dust.

5.2 Grain temperature and mass

Using the dust temperatures from Table 2, we find that the dust cools according to

$$T_{\rm d}({\rm K}) = \frac{5032}{t^{0.346}({\rm d})} \ , \qquad (2)$$

with an uncertainty of ± 0.090 in the exponent of t. Grains having non-zero β, flowing at uniform velocity away from a heating source with constant bolometric luminosity (as would be the case for a CN during the evolutionary phase discussed here), would show a $T_{\rm d} \propto t^{-2/(\beta+4)}$ dependence; the resultant $\beta = 1.78^{+2.03}_{-1.19}$. This is slightly different from zero at the $\sim 2\sigma$ level and hints at the presence of graphitic ($\beta \simeq 1.32$) rather than amorphous carbon grains ($\beta \simeq 0.75$; see also Fig. 10(a)) but we consider various options below.

We recall that there was no evidence for dust on day 33.75 (see above), when the dust temperature would have been $\simeq 1\,490$ K according to Equation (2); Taranova et al. (2014) concluded that dust formed on $\sim$ day 34.75, giving $T_{\rm d} \simeq 1\,470$ K. Extrapolation of Equation (2) leads us to conclude that the dust in V339 Del condensed at a temperature of $\simeq 1\,480 \pm 20$ K. Interestingly, this is well within the range of temperatures (1 150 – 1 690 K) at which graphitic carbon condenses in carbon-rich flows (Ebel 2000, see also discussion in Evans & Rawlings (2008)). This reinforces the conclusion that the dust in V339 Del was graphitic carbon. Furthermore, it is of interest to note that the dust in the classical nova V2326 Cyg condensed at a temperature $1\,410 \pm 15$ K (Lynch et al. 2008), close to the value of the dust condensation temperature we have deduced for V339 Del.

There is further, albeit very circumstantial, evidence for carbon dust in the broadband photometry from the O'Brien Observatory, obtained on day 102.14. In these data there seems to be an excess with respect to the black body continuum at $\sim 11 - 12\,\mu$m (see Fig. 7), although there was no evidence for a feature in this wavelength range in the SOFIA data on day 27.4 (Gehrz et al. 2015). There are a number of possible sources for this excess on day 102.14. The most plausible assignment would be Huα at 12.3719 μm ([Ne II] 12.8135 μm, although sometimes present even in CO novae (see e.g. Evans et al. 1997), would need to be implausibly strong to have a significant effect on broadband data). Another alternative, which would be consistent with the presence of carbon dust, is the 11.1/12.7 μm C−H out-of-plane bending modes in polycyclic aromatic hydrocarbons, commonly seen in nova dust (see e.g. Helton et al. 2011, and references therein).

Irrespective of dust composition, there seems to be some evidence for an increase in dust mass up to $\sim$ day 100, followed by a substantial decline to day ~ 680. The increase may be attributed to grain growth, an increase in the number of emitting grains, or a combination of both these effects. Conversely the subsequent decline must be due to a decline in grain size or decrease in grain number, either of which points to grain destruction on a substantial scale.

5.3 A dust minimum in the visual light curve

It is of interest to correlate the evolution of the dust with the behaviour of the visual light curve. Following visual maximum, the light curve declines uniformly, but the decline becomes distinctly slower after $\sim$ JD2 456 530 ($\sim$ day 12; see Fig. 1(a)); then there is a distinct dip in the light curve as dust forms. We have fitted the light curve immediately before and after the dust dip with a function of the form

$$m_{\rm v} = A + B\ ({\rm JD} - 2455000)$$

and find $A = -95.94 \pm 2.09$ and $B = 0.0669 \pm 0.0013$ day^{-1} (note that B must not be associated with the "speed class" of the nova). We rectified the light curve with this decline to highlight the dust dip (see Fig. 1(b), in which the dust optical depth $\tau = \Delta m_{\rm vis} \times 0.4 \ln 10$ is plotted against the Julian Date). There is a clear maximum in τ, with $\tau \simeq 0.7$, around JD 2 456 580 ($\sim$ day 62). Within the limitations of the cadence of the IR observations, this coincides with maximum grain size and maximum grain mass in Fig. 10(c,d); the duration of the dust phase, as determined by the IR observations, is consistent with the width of the dust dip in Fig. 1(b).

5.4 Grain destruction

Evidence for grain destruction in a nova wind was first noted in the case of nova LW Ser (1978) by Gehrz et al. (1980a). The physical processes associated with grain destruction in nova winds have been discussed by Mitchell, Evans & Bode (1983), Mitchell & Evans (1984), Mitchell, Evans & Albinson (1986) and Rawlings & Evans (1995), in the context of sputtering and chemisputtering of carbon dust, and the effect of annealing carbon dust in the UV radiation field of the nova.

However, more recently the effect of X-radiation on the survival of dust has been the subject of considerable interest in the context of γ-ray bursts (Fruchter et al. 2001), and as V339 Del was an X-ray source (see Section 1), it is of interest to consider the

effect of hard radiation on the survival potential of dust in the environment of V339 Del.

Fruchter et al. (2001) considered the competition between the input of energy into grains by X-radiation, and energy loss by grain radiation and sublimation. They also considered the effect of grain shattering due to electrostatic stress, resulting from grain charging following the ejection of electrons from the $K-$shell of atoms within the grain.

We see from Fig. 10 that, when the dust mass peaked around day 100, the dust temperature was $\sim$ 1 000 K and steadily declined thereafter; is seems unlikely therefore that, at $T \lesssim 1\,000$K, graphitic grains – for which the sublimation temperature is $\gtrsim 1\,800$ K for carbon-rich environments (Lodders & Fegley 1995) – would be subject to evaporation: it is more likely that it is grain shattering by electrostatic stress that destroyed the grains around V339 Del.

Fruchter et al. (2001) found that, whether or not a grain survives following exposure to X-radiation is determined by the parameter E_{51}/D^2_{100}, where E_{51} is the energy radiated in the form of X-rays at 1 keV, normalised to 10^{51} ergs, and D_{100} is the distance of the grains from the X-ray source in units of 100 pc; from Figure 1 of Fruchter et al., grains are shattered if $E_{51}/D^2_{100} \gtrsim 1$.

We suppose that, at the time of maximum grain size, the nova was a SSS with the bulk of the radiation being emitted at X-ray wavelengths. Assuming that the grains are exposed to X-rays for a time Δt, at time t after the eruption, the Fruchter et al. parameter is

$$\frac{E_{51}}{D^2_{100}} \simeq 1.7{\times}10^3 \Phi \left(\frac{L_*}{\mathrm{L}_\odot}\right) \left(\frac{\Delta t}{\mathrm{days}}\right) \left(\frac{t}{\mathrm{days}}\right)^{-2} \left(\frac{V}{500\,\mathrm{km\,s^{-1}}}\right)^{-2}$$

where Φ is the fraction of the nova radiation emitted at 1 keV. Taking $L_* \simeq 8.3 \times 10^5\,\mathrm{L}_\odot$ (Gehrz et al. 2015), $V = 583\,\mathrm{km\,s^{-1}}$, $t \simeq 100$ days, $\Delta t \simeq 100$ days, we find $E_{51}/D^2_{100} \sim 10^6\Phi$. So if $\Phi \gtrsim 10^{-5}$, which seems reasonable, charging of grains by X-radiation is more than sufficient to shatter the grains.

However, while it seems that exposure to X-radiation would destroy the dust, we should express a note of caution in that the Fruchter et al. analysis assumes a power-law for the X-ray source; while this would be valid for the hard X-radiation, it is less so for the near-black body X-ray source appropriate for a CN during the SSS phase (even though pure black body emission does not generally provide a good description of the SSS phase of novae). This issue will be addressed in a forthcoming paper.

Finally, we speculate that the shattering of $\sim$ micron-sized graphitic grains in the way we have suggested might result in the release of significant amounts of polycyclic aromatic hydrocarbon (PAH) fragments, possibly even fullerenes, into the nova environment. If this is the case classical novae may display persistent PAH emission (see Helton et al. 2011, for a summary of PAH emission in novae) for some time after the dust formation phase has apparently come to an end.

6 CONCLUSIONS

We have presented infrared spectroscopy of the classical nova V339 Del.

The IR spectrum is initially dominated by emission by the ejected gas, with H I and low excitation atomic CNO lines being prominent. There is clear evolution in the emission line profiles. The lines are initially ($t \lesssim 37$ days) symmetric, with HWHM $\sim 530\,\mathrm{km\,s^{-1}}$. However, after day 77, they become highly asymmetric, with a strong blue and weak red wing. Later still ($t \gtrsim 600$ days) the emission lines display a castellated structure.

Rapid dust formation occurs around day 34.75, following which the IR emission becomes dominated by the dust. The dust condensation temperature was 1 480 K, consistent with the notion that the dust is graphitic. We find that $\sim 5 \times 10^{-9}\,\mathrm{M}_\odot$ of dust was formed, and that the grains grew to a dimension of a few μm. We further find that both the mass of dust, and the radius of the dust grains, increased rapidly following the formation of dust, peaked around 100 days after eruption, and thereafter declined precipitously. We attribute this to the charging of dust grains by the X-ray emission of V339 Del, causing the grains to shatter due to electrostatic stress.

ACKNOWLEDGEMENTS

We thank Dr Kim Page for valuable information about the early X-ray emission of V339 Del, and the British Astronomical Association and The Astronomer magazine for providing its visual light curve. We also appreciate the referee's supportive comments on this paper.

RDG acknowledges support from the National Aeronautics and Space Administration (NASA) and the United States Air Force. VARMR acknowledges financial support from the Radboud Excellence Initiative. CEW acknowledges partial support from NASA (HST-GO-13828.008-A). SS gratefully acknowledges partial support from both NASA and NSF grants to ASU. The research work at the Physical Research Laboratory is supported by the Department of Space, Government of India. DS is a visiting astronomer at the Infrared Telescope Facility which is operated by the University of Hawaii under contract NNH14CK55B with NASA.

REFERENCES

Ackermann M., et al., 2014, Science, 345, 554
Ahnen M. L., 2015, A&A 582, A67
Banerjee D. P. K., Ashok N. M., 2012, BASI, 40, 243
Banerjee D. P. K., Ashok N. M., Joshi V., Evans A., 2013a, ATel 5337
Banerjee D. P. K., Ashok N. M., Joshi V., Evans A., 2013b, ATel 5404
Banerjee D. P. K., Srivastava Mudit K., Ashok N. M., Venkataraman V., 2016, MNRAS, 455, L109
Beardmore A. P., Osborne J. P., Page K. L., 2013, ATel 5573
Becklin E. E., Capps R. W., 1981, Proc. SPIE, 263, 58
Blanco A., Falcicchia G., Merico F., 1983, Ap. & Sp. Sci., 89, 163
Bode M. F., Evans, A., 2008, Eds Classical Novae, second edition, Cambridge University Press
Cass A. C., Carlon R. L., Corgan D. T., Dykhoff D. A., Gehrz R. D, Shenoy D. P., 2013a, ATel 5434
Cass A. C., Carlon R. L., Corgan D. T., Dykhoff D. A., Gehrz R. D, Shenoy D. P., 2013b, ATel 5604
Chomiuk L., et al., 2014, Nature, 514, 339
Currie M. J., Berry D. S., Jenness T., Gibb A. G., Bell G. S., Draper P. W., 2014, in Astronomical Data Analysis Software and Systems XXIII, eds N. Manset and P. Forshay, Astronomical Society of the Pacific Conference Series, 485, 391
Cushing, M. C., Vacca, W.D., Rayner, J. T., 2004, PASP, 116, 362
Darnley M. J., Bode M. F., Smith R. J., Evans A., 2013, ATel 5279
Das R. K., Banerjee D. P. K., Ashok, N. M., 2009, MNRAS, 398, 375
Deacon N. R., et al., 2014, A&A 563, A129
Ebel D. S., 2000, J. Geophys. Res., 105 10363
Evans A., Rawlings J. M. C., 1994, MNRAS, 269, 427
Evans A., Geballe T. R., Rawlings J. M. C., Scott A. D., 1996, MNRAS, 282, 1049
Evans A., Geballe T. R., Rawlings J. M. C., Eyres S. P. S., Davies J. K., 1997, MNRAS, 292, 192
Evans A., Tyne V. H., Smith O., Geballe T. R., Rawlings J. M. C., Eyres S. P. S., 2005, MNRAS, 360, 1483
Evans A., Gehrz R. D., 2012, BASI, 40, 213
Evans A., Rawlings J. M. C., 2008, in Classical Novae, second edition, eds M. F. Bode, A. Evans, Cambridge University Press
Fruchter A., Krolik J. H., Rhoads J. E., 2001, ApJ, 563, 597
Gehrz R. D., Ney E. P., 1992, Icarus, 100, 162
Gehrz R. D., Grasdalen G. L., Hackwell J. A., Ney E. P., 1980a, ApJ, 237, 855
Gehrz R. D., Hackwell J. A., Grasdalen G. I., Ney E. P., Neugebauer G., Sellgren K., 1980b, ApJ, 239, 570
Gehrz R. D., 2008, in Classical Novae, Eds M. F. Bode, Evans, p. 167, Cambridge University Press
Gehrz R. D., Evans A., Woodward C. E., 2014, in Stella Novae: Future and Past Decades, eds. P. A. Woudt and V. A. R. M. Ribeiro, Astronomical Society of the Pacific Conference Series, 490, 227.
Gehrz R. D., et al., 2015, ApJ, 812, 132
Gehrz R. D., et al., 2016, submitted
Gilman R. C., 1974, ApJS, 28, 397
Haenecour P., Floss C., José, J., Amari S., Lodders K., Jadhav M., Wang A., Gyngard F., 2016, ApJ, 825, 88
Hays E., Cheung T., Ciprini S, 2013 ATel 5302
Helton L. A., Evans A., Woodward C. E., Gehrz, R. D., 2011, in *PAHs and the Universe*, eds C. Joblin and A. G. G. M. Tielens, EAS Publications Series, 46, 407
Helton L. A., et al., 2012, ApJ, 755, 37
Howarth I. D., Murray J., Mills D., Berry D. S., 2004, *DIPSO – A friendly spectrum analysis program*, Starlink User Note 50.24
Hummer D. G., Storey P. J., 1987, MNRAS, 224, 801
Joshi V., Banerjee D. P. K., Ashok N. M., 2014, MNRAS, 443, 559
Krautter J., 2008, in Classical Novae, Eds M. F. Bode, A. Evans, p. 232, Cambridge University Press
Kuulkers E., Page K. L., Osborne J. P., Kuin N. P. M., Sokolovsky K. V., Ness J.-U., 2013, ATel 5283
Linford J. D., et al., 2015, ApJ, 805, 136
Lodders K., Fegley B., 1995, Meteoritics, 30, 661
Lynch D. K., Rudy R. J., Mazuk S., Puetter R. C., 2000, ApJ, 541, 791
Lynch D. K., et al., 2008, AJ, 136, 1815
Martin P., Dubus G., 2013, A&A, 551, A37
Mitchell R. M., Evans A., Bode M. F., 1983, MNRAS, 205, 1141
Mitchell R. M., Evans A., 1984, MNRAS, 209, 945
Mitchell R. M., Evans A., Albinson J. S., 1986, MNRAS, 221, 663
Munari U., et al., 2013a, ATEL 5927
Munari U., Henden A., Dallaporta S., Cherini G., 2013b, IBVS 6080
Naik S., Banerjee D. P. K., Ashok N. M., 2009, MNRAS, 394, 1551
Nakano S., et al., 2013, CBET 3628
Ness J.-U., Schwarz G. J., Page K. L., Osborne J. P., Bode M. F., Shore, S. N., van Rossum D., Starrfield S., Walter F., Woodward C. E., 2013, ATel 5626
Osterbrock D. E., Ferland G. J., 2006, Astrophysical of Gaseous Nebulae and Active Galactic Nuclei, University Science Books
Page K. L., Beardmore A. P., 2013, ATel 5429
Page K. L., Osborne J. P., Beardmore A. P., Kennea J. A., 2013a, ATel 5318
Page K. L., Osborne J. P., Kuin N. P. M., Woodward C. E, Schwarz G. J., Starrfield S., Shore S. N., Walter F. M., 2013b, ATel 5470
Payne-Gaposchkin C., 1957, The Galactic Novae, Dover Publications, New York
Pepin R. O., Palma R. L., Gehrz R. D., Starrfield S., 2011, ApJ, 742, 86
Raj A., Ashok N. M., Banerjee D. P. K., Munari U., Valisa P., Dallaporta S., 2012. MNRAS, 425, 2576
Rawlings J. M. C., Evans A., 1995, Astrophys. Space Sci., 224, 543
Rayner J. T., Toomey D. W., Onaka P. M., Denault A. J., Stahlberger W. E., Vacca W. D., Cushing M. C., Wang, S.,2003, PASP,115, 805,362
Ribeiro V. A. R. M., Munari U., Valisa P., 2013, ApJ, 768, 49
Rudy R. J., Dimpfl W., Lynch D. K., Mazuk S., Venturini C. C., Wilson J. C., Puetter R. C., Perry R. B., 2003, ApJ, 596, 1229
Saikia D. J., Anupama G. C., 2012, Eds Novae from radio to gamma rays, special edition of the Bulletin of the Astronomical Society of India
Schaefer G. H., et al. 2014, Nature, 515, 234
Schmidt G. D., Weymann R. J., Foltz C. B., 1989, PASP, 101, 713
Shenavrin V. I., Taranova O. G., Tatarnikov, A. M., 2013, ATel 5431
Shore S. N., De Gennaro Aquino I., Schwarz G. J., Augusteijn T., Cheung C. C., Walter F. M., Starrfield S., 2013, A&A, 553, A123
Shore S. N., De Gennaro Aquino I., Scaringi S., van Winckel H., 2014, A&A, 570, L4
Shore S. N., et al., 2016, A&A, 590, A123
Slavin A. J., O'Brien T. J., Dunlop J. S., 1995, MNRAS, 276, 353
Skopal A., et al., 2014, A&A, 569, A112
Srivastava M., Ashok N. M., Banerjee D. P. K., Sand D., 2015, MNRAS, 454, 1297
Starrfield S., Iliadis C., Hix W. R., 2016, PASP, 128, 051001
Storey P. J., Hummer D. G., 1995, MNRAS, 272, 41
Stringfellow G. S., Hebb L., Fumagalli M., 2013, ATel 5336
Taranova O. G., Tatarnikov A. M., Shenavrin V. I., Tatarnikova, A. A., 2014, Astron. Lett., 40, 120
Tarasova T. N., Skopal A., 2016, Astron. Lett., 42, 10
Tatischeff V., Hernanz M., 2007, ApJ, 663, L101
Vacca, W. D., Cushing, M. C., Rayner, J. T., 2003, PASP, 115, 389
Warner B., 2008, in Classical Novae, Eds M. F. Bode, A. Evans, p. 16, Cambridge University Press
Weingartner J. C., Draine B. T., Barr D. T., 2006, ApJ, 645, 1188
Williams R. E., 1992, AJ, 104, 725
Williams R., 2012, AJ, 144, 98
Williams S. C., Bode M. F., Darnley M. J., Evans A., Zubko V., Shafter A. W., 2013, ApJ, 777, L32
Woudt, P. A., Ribeiro V. A. R. M., eds Stella Novae: Past and Future Decades, Astronomical Society of the Pacific Conference Series, Volume 490
Young E. T., et al., 2012, ApJ, 749, L17

APPENDIX A: OBSERVED LINE FLUXES

A1 Mt Abu data

The line centres and fluxes were determined by subtracting a continuum and fitting Gaussian functions to the emission line profiles. The uncertainties in the line centres and fluxes arise from the placement of the continuum and the Gaussian fitting. Repeated experiments with slight variations in the assumed continuum, and comparison with line fitting on different dates, showed that the uncertainties in the line centres are typically $\pm 0.0004 - 0.001$ μm, and $\pm 5\%$ to $\pm 12\%$ in the line fluxes.

The line fluxes are listed in Table A1, which lists data to day 26.70, and Table A2, which lists data from day 27.76 onwards. Both Tables give measured wavelengths, suggested identifications and transitions.

A2 MMT data

Line fluxes and centres for each component associated with a given line identification are summarised in Table A3. The components of line profiles where deblended assuming a simple model for the ejecta geometry wherein two Gaussian components where fitted to an emission line using a non-linear least squares technique and the average value of the local continuum. For the Balmer Hα line region, multiple Gaussians were used in an attempt to deblend and fit a rather complex emission profile. Repeated fitting, with the continuum and gaussian full width half maximum as free parameters, suggests that the line profile centers are accurate to $\approx \pm 0.005$Å, with fluxes $\lesssim \pm 5\%$ for most lines, except Hα wherein the uncertainies are $\approx$ 10%. Tentative line identifications and transitions cited in the table are guided by expected emission lines commonly seen in novae in the nebular stage of evolution (e.g., Williams 2012), ionisation states (eV), and atomic line lists contained photoinoization codes[3].

APPENDIX B: PLANCK MEANS AND DUST PROPERTIES

In this section we summarise our determination of the Planck mean absorption efficiencies of carbon dust, together with the determination of dust masses for the case of dust shells that are optically thin in the IR.

B1 Planck means

Most previous estimates of dust masses in CNe (see e.g. Gehrz 2008; Evans & Gehrz 2012, and references therein) are based on the Planck means plotted by Gilman (1974). These in turn are based on a variety of old data and the Planck means are in need of updating. We have used the Planck means measured and tabulated by Blanco et al. (1983). These have been compiled in a systematic fashion and cover the temperature range of interest for CNe.

For carbon, the dependence of the Planck mean absorption efficiency $\langle Q_{\rm abs} \rangle$ on temperature T follows, to a good approximation, a power law of the form

$$\langle Q_{\rm abs} \rangle \simeq A a^{\gamma} T^{\beta} \ ,$$

where A is a constant, a is the radius of the (spherical) grain and β is the β-index for the dust. For carbon grains $\gamma \equiv 1$.

For amorphous carbon (AC) grains, we take Planck mean absorption efficiencies from Blanco et al. (1983), using their "TU" sample. We find that

$$\langle Q_{\rm abs} \rangle = 58.160 \ a \ T^{0.754} \ ,$$

with a in cm, T in K, provides an excellent fit over the temperature range 400–1 700 K; $A = 58.160 \pm 0.754$ and the β-index is 0.754 ± 0.003.

For graphitic carbon (GC) we again take the Planck mean absorption efficiencies from Blanco et al. (1983); these are reasonably fitted over the range 400–1 700 K by

$$\langle Q_{\rm abs} \rangle = 0.653 \ a \ T^{1.315} \ ,$$

with a again in cm and T in K; $A = 0.653 \pm 0.128$ and the β-index is 1.315 ± 0.027.

Both fits are shown in Fig. B1. The AC is clearly well described by a power law but the power law fit to the GR data is rather less stisfactory, particularly at lower temperatures; this is evidenced by the uncertainties in the respective values of A and β. The temperature-dependence for GR is steeper at lower temperatures, and levels off at higher temperatures. Indeed this tendency is clearly evident in Gilman's (1974) Figure 4. However, the assumption of a power law dependence leads to a straight-forward and easily-applied expression for the dust mass and grain radius and, as the deduced dust temperature is at the higher end of the range, we use this simple form here.

B2 Dust mass

B2.1 Carbon grains

For carbon grains the dust emission in the IR, integrated over wavelength, is given by

$$f = \frac{a^2}{D^2} \, N_{\rm gr} \, \frac{\sigma T^4}{\pi} \, \langle Q_{\rm abs} \rangle = \frac{a^2}{D^2} \, \frac{3 M_{\rm d}}{4 \pi a^3 \rho} \, \frac{\sigma T^4}{\pi} \, A a T^{\beta} \ , \qquad \text{(B1)}$$

when the dust shell is optically thin in the IR; the number of emitting grains is

$$N_{\rm gr} = \frac{3 M_{\rm d}}{4 \pi a^3 \rho}$$

and ρ is the density of the grain material. The observed parameter is $\{\lambda f_{\lambda}\}_{\rm max}$ which is related to f by

$$f = 1.359 \ldots \{\lambda f_{\lambda}\}_{\rm max} \ .$$

(see Gehrz & Ney 1992). Rearranging, and using $\rho = 2.25$ g cm^{-3} for carbon, gives

$$M_{\rm d} = 1.359 \, \{\lambda f_{\lambda}\}_{\rm max} \, \frac{D^2}{3} \, \frac{4 \pi \rho}{A \sigma T^{4+\beta}}$$

$$\text{and} \quad \frac{M_{\rm d}}{{\rm M}_{\odot}} = 1.08 \times 10^{20} \left(\frac{\{\lambda f_{\lambda}\}_{\rm max}}{{\rm W \ m^{-2}}} \right) \left(\frac{D}{\rm kpc} \right)^2 \, \frac{1}{A T^{(\beta+4)}} \ , \qquad \text{(B2)}$$

independent of a.

B2.2 Black body grains

In this case $A = 1$, $\beta = \gamma = 0$ and the equivalent of Equation (B1) for the observed dust emission is given by

$$f = \frac{\pi a^2}{D^2} \, N_{\rm gr} \, \frac{\sigma T^4}{\pi} \ , \qquad \text{(B3)}$$

[3] see: http://www.pa.uky.edu/~peter/newpage/

Table A1. Line fluxes measured from Mt Abu data. Earlier data, days 4.73 to 26.70. Fluxes are given in units of 10^{-14} W m^{-2} and are uncorrected for extinction. Uncertainties in the last one, two or three digits are given in brackets; thus 13.0(15) means 13.0 ± 1.5, 469(11) means 469 ± 11 etc.

$\lambda_{\rm obs}$ (μm)	ID, λ_0 (μm)	Transition $\ell - u$	Line flux (10^{-14} W m^{-2}) on days given								
			$t = 4.73$	14.76	15.79	19.78	20.73	22.73	24.72	25.75	26.70
1.0828	He I, 1.0833	^{3}S$-^3$P^o	–	–	–	–	–	–	–	–	–
1.0936	H I, 1.0941	3–6	–	153(5)	–	–	82.7(36)	109(5)	99.3(57)	105(7)	–
1.0946	N I, 1.0946	^{4}S$^o_{3/2}-^4$P	–	–	–		–	–	–	–	122(95)
1.1284	C I, 1.1281	^{1}D$_2-^1$F$^o_3$	–	–	–	–	–	–	–	470(8)	–
1.1293	O I, 1.1290	^{3}P$-^3$D^o	–	–	–	320(5)	313(4)	456(6)	392(7)	–	469(11)
1.1300	N I, 1.1297	^{4}D$^o_{1/2}-^4$P$_{1/2}$	–	353(8)	433(9)	–	–	–	–	–	–
	O I, 1.1301	^{5}P$_2-^5$S$^o_2$	–	–	–	–	–	–	–	–	–
	C I, 1.1301	^{3}P$^o_1-^3$D$_2$	–	–	–	–	–	–	–	–	–
	N I, 1.1301	^{4}P$^o_{1/2}-^4$P$_{1/2}$	–	–	–	–	–	–	–	–	–
	N I, 1.1300	^{4}P$^o_{5/2}-^4$D	–	–	–	–	–	–	–	–	–
	N I, 1.1303	^{2}P$^o_{1/2}-^2$D	–	–	–	–	–	–	–	–	–
	N I, 1.1304	^{4}D$^o_{3/2}-^4$D$_{1/2}$	–	–	–	–	–	–	–	–	–
1.1463			–	–	–	–	–	–	–	–	–
1.1619	C I, 1.1618	^{3}D$-^3$D^o	–	–	24.2(12)	9.17(69)	–	–	3.92(50)	–	–
	C I, 1.1622	^{3}D$-^3$D^o	–	–	–	–	–	–	–	–	–
1.1654	C I, 1.1651	^{3}D$_2-^3$D$^o_1$	–	75.2()	–	29.3(36)	27.9(16)	35.0(92)	24.2(1.63)	26.4(1.3)	31.7(94)
1.1662	C I, 1.1662	^{3}S$-^3$P^o	–		48.0(58)	–	–	–	–	–	–
1.1758	C I, 1.1758	^{3}D$_2-^3$F$^o_3$	–	151(3)	160(4)	91.5(18)	76.5(35)	92.5(18)	73.7(11)	74.9(14)	80.4(10)
	C I, 1.1757	^{3}D$_3-^3$F$^o_4$	–	–	–	–	–	–	–	–	–
1.1863	C I, 1.1864	^{3}P$_2-^3$D$^o_3$	–	49.4(25)	–	–	–	–	–	–	–
	C I, 1.1864	^{3}P$_2-^3$D$^o_2$	–	–	–	–	–	–	–	–	–
	C I, 1.1866	D$_1-^3$P$^o_1$	–	–	–	–	–	–	–	–	–
	N I, 1.1861	^{4}S$^o_{3/2}-^4$P$_{3/2}$	–	–	–	–	–	–	–	–	–
1.1887			–	–	–	16.3(13)	18.2(18)	21.9(11)	16.8(7)	13.7(9)	19.7(10)
1.2087			–	–	–	–	–	–	–	–	12.5(14)
1.2191			–	–	–	–	–	–	–	–	4.19(34)
1.2300			–	–	–	–	–	–	–	–	8.76(51)
1.2466	N I, 1.2473	^{2}D$^o_{5/2}-^2$F$_{7/2}$	–	26.4(52)	31.8 (37)	10.5(13)	11.4(23)	11.7(8)	11.5(15)	11.0(14)	11.2(10)

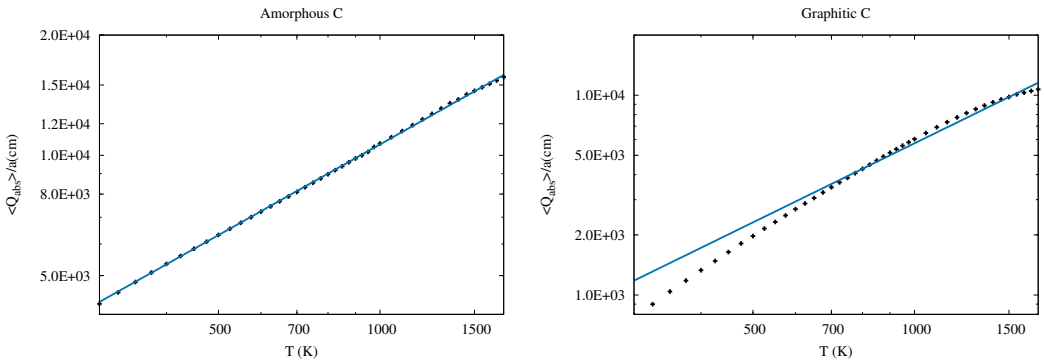

Figure B1. Fit of functions of the form $\langle Q_{\rm abs} \rangle = AaT^{\beta}$ to laboratory Planck mean data in Blanco et al. (1983). Left, amorphous carbon, right, graphitic carbon. The fits are confined to the temperature range 400 – 1700 K.

Rearranging gives

$$M_{\rm d} \;=\; 1.812\, D^2\, \{\lambda f_\lambda\}_{\rm max}\; \frac{\pi a \rho}{\sigma T^4}$$

$$\text{and} \quad \frac{M_{\rm d}}{\rm M_\odot} \;\simeq\; 4.805 \times 10^{16}\; \frac{a\rho\, D^2_{\rm kpc}\, \{\lambda f_\lambda\}_{\rm max}}{T^4} \quad . \text{(B4)}$$

Note that in this case $M_{\rm d}$ depends on a.

This paper has been typeset from a TEX/LATEX file prepared by the author.

Table A1. Continued. Line fluxes measured from Mt Abu data. Earlier data, days 4.73 to 26.70. Fluxes are given in units of 10^{-14} W m^{-2} and are uncorrected for extinction. Uncertainties in the last one, two or three digits are given in brackets; thus 13.0(15) means 13.0 ± 1.5, 469(11) means 469 ± 11 etc.

$\lambda_{\rm obs}$ (μm)	ID, λ_0 (μm)	Transition $\ell - u$	Line flux (10^{-14} W m^{-2}) on days given								
			$t = 4.73$	14.76	15.79	19.78	20.73	22.73	24.72	25.75	26.70
1.2509			–	–	–	–	–	–	–	–	–
1.2586	N I, 1.2586	$^2F_{7/2}-D^o$	–	46.5(10)	49.1(11)	17.6(16)	17.3(28)	17.6(10)	17.1(38)	16.5(4)	14.7(10)
	C I, 1.2585	$^3P_1-^3P^o_2$	–	–	–	–	–	–	–	–	–
	N I, 1.2585	$^2D^o_{5/2}-^2F_{5/2}$	–	–	–	–	–	–	–	–	–
1.2809			–	–	–	–	–	–	–	–	–
1.2823	H I, 1.2822	3–5	8.40(107)	213(3)	261(4)	175(2)	170(3)	198(2)	202(2)	218(2)	224(2)
1.2975	N I, 1.2973	$^2P-^2D^o$	–		3.582(32)	–	–	–	–	–	–
1.3172	N I, 1.3177	$^2D_{3/2}-^2D^o_{5/2}$	–	29.0(6)	–	14.3(14)	11.9(23)	–	13.0(15)	13.0(15)	15.2(18)
	N I, 1.3176	$^2D_{5/2}-^2D^o_{5/2}$	–	–	–	–	–	–	–	–	–
1.5268			–	–	–	1.29(9)	–	–	–	–	1.77(10)
1.5348			–	–	3.46(20)	1.82(11)	–	–	1.81(8)	–	1.77(9)
1.5447			–	–	4.84(20)	2.80(12)	–	3.06(14)	2.56(8)	2.54(14)	2.33(9)
1.5568	H I,1.5561	4–16	–	9.23(28)	9.64(22)	5.56(13)	–	6.33(15)	5.92(10)	6.18(17)	5.67(11)
1.5707	H I,1.5705	4–15	–	7.88(31)	9.07(24)	5.14(14)	–	5.82(16)	5.39(10)	4.99(17)	4.58(10)
1.5748		–	–	–	–	–	–	–	–	–	–
1.5789			–	–	1.47(16)	0.71(9)	–	0.69(7)	0.58(7)	0.55 (7)	–
1.5847	H I,1.5885	4–14	–	11.9(3)	12.3(2)	6.63(13)	–	6.55(15)	6.19(9)	5.95(16)	–
1.6021			–	7.68(28)	7.75(23)	3.37(9)	–	3.12(7)	2.89(7)	2.85(7)	2.95(16)
1.6054		–	–	–	–	–	–	–	–	–	–
1.6115	H I, 1.6114	4–13	–	10.7(2)	11.3(2)	6.58(14)	–	6.63(15)	6.87(10)	7.05(17)	6.69(17)
1.6329			–	–	–	0.44(9)	–	–	–	–	–
1.6142		–	–	–	–	–	–	–	–	–	–
1.6416	H I, 1.6412	4–12	–	21.8(5)	21.67(113)	10.2(3)	–	10.5(6)	10.4(4)	10.3(2)	10.5(2)
1.6499			–	–	–	–	–	0.69(7)	–	–	–
1.6711			–	–	–	0.95(7)	–	–	–	–	–
1.6808	H I, 1.6811	4–11	–	19.7(31)	15.3(7)	9.38(28)	–	10.5(4)	10.6(3)	10.2(3)	11.7(6)
1.6826			–	–	–	–	–	–	–	–	–
1.6892	C I, 1.6895	$^1D_2-^1F^o_3$	2.69(25)	28.0(29)	44.4(10)	–	–	22.1(9)	23.3(4)	21.9(5)	18.8(5)
1.7058			–	–	–	1.57(9)	–	–	–	–	–
1.7244			–	–	–	–	–	–	–	–	–
1.7251			–	–	–	3.71(25)	–	3.59(39)	3.29(41)	2.71(30)	2.72(16)
1.7362	H I, 1.7367	4–10	–	–	–	22.5(4)	–	25.4(11)	24.7(5)	23.1(6)	19.0(6)
1.7450			–	–	–	–	–	13.0(5)	–	11.0(2)	–
1.7563			–	–	–	–	–	4.53(29)	–	4.75(21)	–
1.7667			–	–	–	–	–	11.6(10)	9.52(50)	7.98(63)	–
1.9741			–	–	–	1.71(6)	–	1.25(6)	2.19(10)	1.43(4)	–
2.0599	He I, 2.0587	$^1S_0-^1P^o_1$	–	–	–	1.546)	2.13(9)	1.26(9)	1.77(8)	1.90(8)	1.87(7)
2.0757			–	–	–	0.32(4)	0.37(7)	–	–	–	–
2.0890			–	–	–	0.47(0.04)	0.70(8)	–	0.66(4)	0.54(4)	0.81(4)
2.1029	C I, 2.1029	$^1S-^1P^o$	–	1.50(14)	2.21(17)	0.66(4)	0.74(5)	–	0.45(3)	0.35(3)	0.43(4)
2.1235			–	5.85(23)	7.34(13)	2.81(6)	3.07(7)	2.56(9)	2.76(7)	2.24(5)	2.13(6)
2.1492			–	–	3.32(12)	–	–	1.28(7)	1.33(6)	–	0.76(3)
2.1505			=[ii0–	–	–	–	1.46(6)	–	–	1.01(4)	–
2.1645		–	–	–	–	–	–	–	–	–	–
2.1667	H I, 2.1661	4–7	—	22.5(35)	20.9(2)	–	15.3(2)	14.1(2)	18.0(2)	15.5(2)	16.6(3)
2.2153			–	2.44(18)	1.87(17)	0.56(5)	–	–	0.41(3)	0.28(3)	0.44(5)
2.2891			–	1.17(13)	–	–	–	–	–	–	–
2.2918	C I 2.2913	$^1S_0-^1P^o_1$	–	–	2.33(18)	1.12(5)	–	–	0.86(32)	0.73(3)	0.76(4)
2.3158			–	–	0.63(8)	–	–	–	–	–	–

Table A2. Line fluxes measured from Mt Abu data. Later data, days 27.76 to 102.66. Fluxes are given in units of 10^{-14} W m^{-2} and are uncorrected for extinction. Uncertainties in the last one, two or three digits are given in brackets; thus 13.0(15) means 13.0 ± 1.5, 469(11) means 469 ± 11 etc.

$\lambda_{\rm obs}$ (μm)	ID, λ_0 (μm)	Transition $\ell - u$	Line flux (10^{-14} W m^{-2}) on days given								
			$t = 27.76$	31.82	33.75	36.82	37.69	77.79	78.71	101.72	102.66
1.0828	He I, 1.0833	^{3}S$-^3$P^o	–	–	–	192(3)	150(2)	–	8.57(74)	6.89(16)	6.89(23)
1.0936	H I, 1.0941	3–6	–	183(8)	–	149(3)	135(2)	–	–	1.21(17)	0.35(11)
1.0946	N I, 1.0946	^{4}S$^o_{3/2}-^4$P	–	–	–	–	–	–	–	–	0.36(10)
1.1284	C I, 1.1281	^{1}D$_2-^1$F$^o_3$	425(4)	798(9)	–	–	625(5)	1.75 (7)	1.61(7)	0.82(3)	0.71(3)
	O I, 1.1290	^{3}P$-^3$D^o	–	–	–	–	–	–	–	–	–
1.1300	N I, 1.1297	^{4}D$^o_{1/2}-^4$P$_{1/2}$	–	–	–	–	–	–	–	–	–
	O I, 1.1301	^{5}P$_2-^5$S$^o_2$	–	–	–	–	–	–	–	–	–
	C I, 1.1301	^{3}P$^o_1-^3$D$_2$	–	–	–	–	–	–	–	–	–
	N I, 1.1301	^{4}P$^o_{1/2}-^4$P$_{1/2}$	–	–	–	–	–	–	–	–	–
	N I, 1.1300	^{4}P$^o_{5/2}-^4$D	–	–	–	–	–	–	–	–	–
	N I, 1.1303	^{2}P$^o_{1/2}-^2$D	–	–	–	–	–	–	–	–	–
	N I, 1.1304	^{4}D$^o_{3/2}-^4$D$_{1/2}$	–	–	–	–	–	–	–	–	–
1.1463			–	–	–	–	–	0.168(55)	–	–	–
1.1619	C I, 1.1618	^{3}D$-^3$D^o	–	–	–	–	–	–	–	–	–
	C I, 1.1622	^{3}D$-^3$D^o	–	–	–	–	–	–	–	–	–
1.1654	C I, 1.1651	^{3}D$_2-^3$D$^o_1$	18.8(35)	25.0(18)	23.4(10)	–	17.0 (6)	–	–	–	–
1.1662	C I, 1.1662	^{3}S$-^3$P^o	–	–	–	–	–	–	–	–	–
1.1758	C I, 1.1758	^{3}D$_2-^3$F$^o_3$	56.5(31)	73.0(87)	67.5(24)	–	50.3(53)	0.18(6)	0.31(8)	0.14(3)	–
	C I, 1.1757	^{3}D$_3-^3$F$^o_4$	–	–	–	–	–	–	–	–	–
1.1863	C I, 1.1864	^{3}P$_2-^3$D$^o_3$	–	–	–	–	–	–	–	–	–
	C I, 1.1864	^{3}P$_2-^3$D$^o_2$	–	–	–	–	–	–	–	–	–
	C I, 1.1866	D$_1-^3$P$^o_1$	–	–	–	–	–	–	–	–	–
	N I, 1.1861	^{4}S$^o_{3/2}-^4$P$_{3/2}$	–	–	–	–	–	–	–	–	–
1.1887			11.3(35)	30.7(47)	19.6(11)	–	11.6(6)	–	–	0.096(30)	–
1.2087			–	–	18.1(16)	–	4.34(62)	–	–	–	–
1.2191			–	–	–	–	–	–	–	–	–
1.2300			–	3.52(32)	–	–	–	–	–	–	–
1.2466	N I,1.2473	^{2}D$^o_{5/2}-^2$F$_{7/2}$	7.24(93)	10.0(12)	14.3(11)	7.35(51)	8.56(18)	–	–	–	
1.2509			–	–	–	–	–	–	–	–	0.20(2)
1.2586	N I, 1.2586	^{2}F$_{7/2}-$D	11.3(12)	13.0(3)	18.2(14)	9.82(69)	11.0(2)	–	–	–	–
	C I, 1.2585	^{3}P$_1-^3$P$^o_2$	–	–	–	–	–	–	–	–	–
	N I, 1.2585	^{2}D$^o_{5/2}-^2$F5/2	–	–	–	–	–	–	–	–	–
1.2809			–	–	–	–	–	1.63(5)	1.77(5)	1.54(4)	1.57(3)
1.2823	H I, 1.2822	3–5	192(2)	230(1)	252(3)	214(2)	251(1)	–	–	–	–
1.2975	N I, 1.2973	^{2}P$-^2$D^o	–	–	–	–	–	–	–	–	–
1.3172	N I, 1.3177	^{2}D$_{3/2}-^2$D$^o_{5/2}$	11.1 (11)	8.9(12)	–	8.42(65)	10.6(2)	–	–	–	–
	N I, 1.3176	^{2}D$_{5/2}-^2$D$^o_{5/2}$	–	–	–	–	–	–	–	–	–
1.5268	–	–	–	–	–	–	0.42(4)	–	–	–	–
1.5348			1.74(10)	1.4 (1)	1.23(8)	–	0.88(5)	–	–	–	–
1.5447			2.45(10)	1.74(10)	1.79(8)	–	1.29(5)	–	–	–	–
1.5568	H I, 1.5561	4–16	5.68(12)	4.79 (12)	4.28(9)	3.40(7)	3.13(6)	–	–	–	–
1.5707	H I, 1.5705	4–15	4.67(12)	4.03(12)	3.68(9)	2.86(2)	2.18(5)	–	–	–	–
1.5748			–	–	–	–	–	–	–	–	0.025(4)
1.5789			–	–	–	–	–	–	–	–	–
1.5847	H I, 1.5885	4–14	5.44(11)	4.37(11)	4.14(9)	3.29(7)	3.31(8)	0.17(1)	–	–	0.119(14)
1.6021			2.53(10)	1.48(10)	1.26(8)	0.90(6)	0.99(7)	–	–	–	–
1.6054			–	–	–	–	–	–	–	–	0.027(3)
1.6115	H I, 1.6114	4–13	6.28(11)	5.30(12)	4.53(9)	3.94(7)	3.52(8)	–	–	–	–
1.6142			–	–	–	–	–	–	–	–	0.092(16)
1.6329			–	–	–	–	–	–	–	–	–
1.6416	H I, 1.6412	4–12	8.60(15)	7.65 (12)	6.93(16)	5.86(56)	5.62(8)	–	–	–	0.183(16)
1.6499			–	–	0.318(66)	–	–	–	–	–	–
1.6711			–	–	0.428(72)	–	–	–	–	–	–

Table A2. Continued. Line fluxes measured from Mt Abu data. Later data, days 27.76 to 102.66. Fluxes are given in units of 10^{-14} W m^{-2} and are uncorrected for extinction. Uncertainties in the last one, two or three digits are given in brackets; thus 13.0(15) means 13.0 ± 1.5, 469(11) means 469 ± 11 etc.

$\lambda_{\rm obs}$ (μm)	ID, λ_0 (μm)	Transition $\ell - u$	Line flux (10^{-14} W m^{-2}) on days given								
			$t = 27.76$	31.82	33.75	36.82	37.69	77.79	78.71	101.72	102.66
1.6808	H I, 1.6811	4–11	10.73(39)	8.90(31)	8.04(26)	7.61(98)	6.81(42)	–	–	–	0.220(24)
1.6826			–	–	–	–	–	0.327(10)	–	–	–
1.6892	C I, 1.6895	^{1}D$_2$–^{1}F$^o_3$	16.9(4)	12.6(3)	11.7(3)	9.59(100)	9.06(42)	–	–	–	0.087(5)
1.7058			–	–	–	–	–	–	–	–	–
1.7247			2.02(4)	1.95(14)	1.35(7)	–	–	–	–	–	–
1.7362	H I, 1.7367	4–10	18.3(6)	17.3(3)	14.1(2)	13.2(7)	13.4(4)	0.276(11)	–	–	0.355(20)
1.7450			3.46(53)	–	–	–	–	–	–	–	–
1.7563			–	–	–	–	–	–	–	–	–
1.7667			–	–	–	–	–	–	–	–	–
1.9741			1.76(9)	1.39(6)	1.24(15)	–	0.863(68)	–	–	–	–
2.0599	He I, 2.0587	^{1}S$_0$–^{1}P$^o_1$	1.57 (7)	2.04(16)	4.21(22)	6.67(18)	5.48(7)	–	–	–	0.107(10)
2.0757			–	–	–	–	–	–	–	–	–
2.0890			0.51(5)	0.57(4)	0.65(5)	0.47(15)	0.47(7)	–	–	–	–
2.1029	C I, 2.10289	^{1}S–^{1}P^o	0.29(4)	0.221(25)	–	–	–	–	–	–	–
2.1235			1.88(7)	1.50 (7)	1.79(10)	1.04(5)	0.718(41)	–	–	–	–
2.1492			–	–	–	–	–	–	–	–	–
2.1505			–	0.841(7)	–	0.525(53)	0.447(41)	–	–	–	–
2.1645			–	–	–	–	–	0.491(24)	–	–	0.366(15)
2.1667	H I, 2.1661	4–7	15.8(3)	15.7(2)	14.8(2)	14.9(2)	13.0 (1)	–	–	–	–
2.2153			–	–	–	–	–	–	–	–	–
2.2891			–	–	–	–	–	–	–	–	–
2.2918	C I, 2.2913	^{1}S$_0$–^{1}P$^o_1$	–	0.479(22)	–	0.345(31)	0.358(23)	–	–	–	–
2.3158			–	–	–	–	–	–	–	–	–

Table A3. V339 Del optical line fluxes measured from the MMT spectra on day 672.50. Fluxes are uncorrected for extinction.

$\lambda_{\rm obs}$ (Å)	ID, λ_0 (Å, air)	Transition $l-u$	Line flux (10^{-17} W m^{-2})
3963.381	Hϵ, 3970.072	$2-7$	10.04
3972.851	Hϵ, 3970.072	$2-7$	5.90
4094.305	Hδ, 4101.135	$2-6$	21.77
4105.861	Hδ, 4101.135	$2-6$	14.17
4261.049	C II, 4267.183	^{2}D$-^2$F$_0$	3.38
4273.072	C II, 4267.183	^{2}D$-^2$F$_0$	2.26
4334.038	Hγ, 4340.463	$2-5$	23.40
4354.927	Hγ, 4340.463	$2-5$	29.52
4344.003	[O III], 4363.209	^{1}D$-^1$S	11.02
4370.276	[O III], 4363.209	^{1}D$-^1$Ss	16.74
4632.792	N III, 4640.640	^{2}P$_0-^2$D	18.30
4646.433	N III, 4640.640	^{2}P$_0-^2$D	13.77
4678.127	He II, 4685.710	$3-4$	12.07
4691.931	He II, 4685.710	$3-4$	8.66
4853.992	Hβ, 4861.325	$2-4$	54.77
4867.393	Hβ, 4861.325	$2-4$	38.87
4951.556	[O III], 4958.911	^{3}P$-^1$D	482.3
4965.698	[O III], 4958.911	^{3}P$-^1$D	320.8
4999.424	[O III], 5006.843	^{3}P$-^1$D	1453.0
5013.692	[O III], 5006.843	^{3}P$-^1$D	973.0
5168.903	[Fe VI], 5176.040	^{4}F$-^2$G	2.25
5191.028	[Fe VI], 5176.040	^{4}F$-^2$G	2.46
5405.475	He II, 5411.520	$4-7$	1.18
5418.364	He II, 5411.520	$4-7$	1.08
5526.680	Ar II, 5534.990	^{4}D$-^4$P$_0$	0.92
5541.127	Ar II, 5534.990	^{4}D$-^4$P$_0$	0.69
5670.579	[Fe VI], 5676.950	^{4}F$-^4$P	4.21
5685.666	[Fe VI], 5676.950	^{4}F$-^4$P	2.47
5745.688	[N II], 5754.644	^{1}D$-^1$S	6.66
5762.683	[N II], 5754.644	^{1}D$-^1$S	4.14
5866.875	He I, 5875.966	^{3}P$_0-^3$D	6.93
5882.082	He I, 5875.966	^{3}P$_0-^3$D	5.31
5932.956	N I, 5931.780	^{3}P$-^3$D$_0$	0.91
5948.923	N I, 5931.780	^{3}P$-^3$D$_0$	0.37
6076.424	[Ca V], 6086.400 + [Fe VII], 6086.290	^{3}P$-^1$D; ^{3}F$-^1$D	1.20
6096.129	[Ca V], 6086.400 + [Fe VII], 6086.290	^{3}P$-^1$D; ^{3}F$-^1$D	1.09
6292.857	[O I], 6300.304	^{3}P$-^3$D	26.10
6307.521	[O I], 6300.304	^{3}P$-^3$D	16.46
6356.264	[O I], 6363.766 + [Fe X], 6374.500	^{3}P$-^1$D; ^{2}P$_0-^2$P$_0$	8.93
6371.086	[O I], 6363.766 + [Fe X], 6374.500	^{3}P$-^1$D; ^{2}P$_0-^2$P$_0$	5.55
6536.497	[N II], 6548.040	^{3}P$-^1$D	111.60
6559.453	[N II], 6548.040	^{3}P$-^1$D	153.50
6549.564	Hα, 6562.80 + He II, 6560.10	$2-3; 4-6$	221.30
6582.781	Hα, 6562.80 + He II, 6560.10	$2-3; 4-6$	305.00
6571.919	[N II], 6583.460	^{3}P$-^1$D	458.20
6594.550	[N II], 6583.460	^{3}P$-^1$D	239.90
6669.174	He I, 6678.152	^{1}P$_0-^1$D	2.23
6685.912	He I, 6678.152	^{1}P$_0-^1$D	1.83
7054.257	He I, 7065.215	^{3}P$_0-^3$D	1.92
7071.989	He I, 7065.215	^{3}P$_0-^3$D	1.68